An assessment of ballistic hazard and risk from Upper Te Maari, Tongariro, New Zealand

---

A thesis

submitted in partial fulfilment of the requirements for the degree

of

Master of Science in Geology

at

The University of Canterbury

by

Rebecca Hanna Fitzgerald

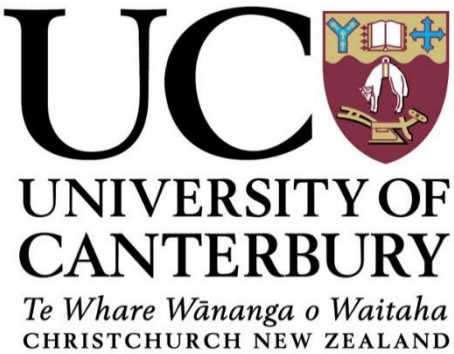

University of Canterbury

2014

TABLE OF CONTENTS

TABLE OF FIGURES

TABLE OF TABLES

ABSTRACT

Explosive volcanic eruptions frequently expel ballistic projectiles, producing a significant proximal hazard to people, buildings, infrastructure and the environment from their high kinetic and thermal energies. Ballistic hazard assessments are undertaken as a risk mitigation measure, to determine probabilities of eruptions occurring that may produce ballistics, identify areas and elements likely to be impacted by ballistics, and the potential vulnerabilities of elements to ballistics.

The 6 August, 2012 hydrothermal eruption of Upper Te Maari Crater, Tongariro, New Zealand ejected blocks over a 6 km^2 area, impacting ~2.6 km of the Tongariro Alpine Crossing (TAC), a walking track hiked by ~80,000 people a year, and damaging an overnight hut along the track. In this thesis ballistic hazard and risk from Upper Te Maari Crater are assessed through a review of its eruptive history, field and orthophoto mapping of the 6 August ballistic impact distribution, forward modelling and analysis of possible future eruption scenarios using a calibrated 3D ballistic trajectory model, and analysis of the vulnerability of hikers along the impacted Tongariro Alpine Crossing.

Orthophoto mapping of the 6 August ballistic impact crater distribution revealed 3,587 impact craters with a mean diameter of 2.4 m. However, field mapping of accessible regions indicated an average of at least four times more observable impact craters and a smaller mean crater diameter of 1.2 m. By combining the orthophoto and ground-truthed impact frequency and size distribution data, it is estimated that approximately 13,200 ballistic projectiles were generated during the eruption.

Ballistic impact distribution was used to calibrate a 3D ballistic trajectory model for the 6 August eruption. The 3D ballistic trajectory model and a series of inverse models were used to constrain the eruption directions, angles and velocities. When combined with eruption observations and geophysical observations and compared to the mapped distribution, the model indicated that the blocks were ejected in five variously directed eruption pulses, in total lasting 19 seconds. The model successfully reproduced the mapped impact distribution using a mean initial particle velocity of 200 m/s with an accompanying average gas flow velocity over a 400 m radius of 150 m/s.

Assessment of the vulnerability of hikers to ballistics from the August eruption along the TAC utilised the modelled spatial density of impacts and an assumption that an average ballistic impact will cause serious injury or death (casualty) over an 8 m^2 area. It is estimated that the probability of casualty ranged from 1% to 16% along the affected track (assuming an eruption during the time of exposure). Future ballistic hazard and vulnerability along the TAC are also assessed through application of the calibrated model. A magnitude larger eruption (than the 6 August) in which 10x more particles were ejected, doubled the affected length of the TAC and illustrated that the probability of casualty could reach 100% in localised areas of the track. In contrast, ballistics ejected from a smaller eruption did not reach the track as was the case with the 21 November 2012 eruption. The calibrated ballistic model can therefore be used to improve management of ballistic hazards both at Tongariro and also, once recalibrated, to other volcanoes worldwide.

UNIVERSITY OF CANTERBURY
Te Whare Wānanga o Waitaha
CHRISTCHURCH NEW ZEALAND

Deputy Vice-Chancellor's Office
Postgraduate Office

Co-Authorship Form

This form is to accompany the submission of any PhD thesis that contains research reported in co-authored work that has been published, accepted for publication, or submitted for publication. A copy of this form should be included for each co-authored work that is included in the PhD thesis. Completed forms should be included at the front (after the thesis abstract) of each copy of the thesis submitted for examination and library deposit (including electronic copy).

Please indicate the chapter/section/pages of this thesis that are extracted from co-authored work and provide details of the publication or submission from the extract comes:

Chapter 3

Fitzgerald RH, Tsunematsu K, Kennedy BM, Breard ECP, Lube G, Wilson TM, Jolly AD, Pawson J, Rosenberg MD, Cronin SJ 2014. The application of a calibrated 3D ballistic trajectory model to ballistic hazard assessments at Upper Te Maari, Tongariro. Journal of Volcanology and Geothermal Research http://dx.doi.org/10.1016/j.jvolgeores.2014.04.006

Please detail the nature and extent (%) of contribution by the PhD candidate:

Vast majority of field mapping (95%), orthophoto mapping (95%) and data analysis (90%), as well as writing the vast majority of the paper (80%). Collaboration with co-authors was required as part of data collection, modelling and manuscript preparation, which I outline here:

- Kae Tsunematsu, Mount Fuji Research Institute, collaborator. Kae ran the ballistic trajectory model from her computer in Japan, though using my field data and with me leading the source parameter selection and completing analysis

- Eric Breard, Massey University, collaborator. Eric provided additional data (~20 crater locations) collected that outlined the edge of the ballistic field to the east and south, outside the orthophoto extent and which I was not able to reach in the field
- Jo Pawson, University of Canterbury, collaborator. Field assistant - mapping.
- Michael Rosenberg, GNS Science, collaborator. Provided block data GNS collected near the crater and around Ketetahi Hut in the days immediately following the eruption)
- Ben Kennedy (senior supervisor; UC), Tom Wilson (co-supervisor; UC), Art Jolly (associate supervisor; GNS Science) and Gert Lube (associate supervisor; Massey University) provided discussion on data analysis and interpretation and conceptual development of the research as part of normal academic supervisory relationship
- Shane Cronin, Massey University, collaborator. Provided discussion on data analysis and interpretation.

Certification by Co-authors:
If there is more than one co-author then a single co-author vcan sign on behalf of all
The undersigned certifys that:

- The above statement correctly reflects the nature and extent of the PhD candidate's contribution to this co-authored work
- In cases where the PhD candidate was the lead author of the co-authored work he or she wrote the text

Name:	Signature:	Date:
Tom Wilson		10/6/14

ACKNOWLEDGEMENTS

Firstly thanks to my amazing supervisors Ben Kennedy, Tom Wilson, Art Jolly and Gert Lube for all the support, guidance and discussions. Ben and Tom, thank you for creating such an awesome thesis topic for me, for always being so positive and enthusiastic, for all the opportunities you've given me and for dealing with all my last-minute submissions (sorry!). I also want to acknowledge Kae Tsunematsu without whom I would not have any models to present. Thank you for always being so kind and understanding when I would ask for models to be rerun!

I would like to acknowledge my field assistants Emma Rhodes, James Cowlyn, Matt Edwards and Aaron Lister. Thanks for being so willing to help out and for always carrying the heavy stuff - especially the DCP!

To everybody in office 401 – I don't think there has ever been a better office. Thanks for the laughs, the entertaining office pranks, my terrarium, free reign over the heater, and most of all for helping me at the end – I honestly could not have finished without you. Additionally thanks to all the other staff and students who make the department such an awesome place.

Thanks to the Department of Conservation, especially Harry Keys, Ngāti Hikairo ki Tongariro and Ngāti Tuwharetoa for allowing me to carry out fieldwork on Tongariro.

This project was supported by funding from the Mason Trust and Project Tongariro, without which fieldwork would not have been possible.

Thank you to the technical and administrative staff who have helped me along the way, in particular Kerry Swanson, Sacha Baldwin-Cunningham, Janet Brehaut, Janet Warburton and Pat Roberts.

And last but not least, a big thank you goes to my family for always supporting and encouraging me, for all the late night food deliveries, for the motivating phone calls when I really needed it, and for just being generally awesome.

CHAPTER 1: INTRODUCTION

1.1 CONTEXT OF STUDY

Volcanic eruptions produce a number of hazards that can impact society. Of these, volcanic ballistic projectiles, frequently ejected from explosive eruptions, represent a significant proximal hazard to people, buildings, infrastructure and the surrounding environment. Their high impact and sometimes thermal energies can result in death or serious injury (Blong 1984; Baxter and Gresham 1997), building damage (Pistolesi et al. 2008; Wardman et al. 2012; Jenkins et al. 2014), ignition of both buildings and the environment they impact (Zobin et al. 2002; Alatorre-Ibargüengoitia et al. 2006; Wardman et al. 2012), and damage to the surrounding environment. The impacts of volcanic hazards such as ballistic projectiles can be reduced through volcanic risk management including volcanic hazard and risk assessments, volcanic surveillance and risk mitigation strategies such as land use planning, eruption warnings and volcanic engineering.

Hazard assessments are undertaken to determine the likelihoods of events occurring that may produce hazards and the areas that may be impacted by these hazards (Thouret et al. 2000; Alatorre-Ibargüengoitia et al. 2006; 2012). The likelihood of consequences (e.g. death or serious injury) from exposure to the hazard are determined in risk assessments (Blong 1996). For ballistic risk assessments this may involves a review of the volcanic eruption history to determine past eruption magnitudes and frequencies to inform probabilities of future eruptions; determining the nature and extent of past ballistic distributions through field mapping or remote sensing, and possible future distributions through ballistic trajectory modelling; and identifying assets in the area that may be impacted, such as people and buildings, and their vulnerability to the hazard (e.g. likelihood of death or damage) (Nadim 2013).

Ballistic hazard and risk assessments are used as the basis for risk management strategies, such as implementing evacuation and exclusion zones, designing engineering solutions for the built environment, and land use planning (Sparks et al. 2013). However, creating a complete assessment can be challenging, requiring a large amount of information which can

be challenging to collect. For example, field mapping is time consuming, labour intensive and can be hazardous due to the risk of further eruption; subsequent ash deposition can obscure impact craters; and remote mapping may be limited by image resolution. As a result, those managing the risk of ballistic hazards at active volcanoes have tended to use a precautionary hazard assessment approach, where a concentric hazard zone is used to account for uncertainty in directionality of eruption pulses. The radius of the zone is typically identified by the maximum travel distance of a ballistic for various magnitude eruption scenarios, informed by field surveys or ballistic trajectory models (Alatorre-Ibargüengoitia et al. 2006; 2012; Jolly and Taig 2012). However, this can lead to large areas being classified potentially hazardous which can compromise social and economic activities within those areas, especially if risk management treatments are applied. Balancing the risk to life against the impact of risk management treatments is a substantial issue for contemporary volcanic risk management (Sparks et al. 2013). Therefore there is increasing need and emphasis placed on producing quantifiable, transparent and customised ballistic hazard and risk assessments, especially in situations where social and economic activities require access to hazardous zones.

A recent example of this was the 6 August, 2012 hydrothermal eruption at the Upper Te Maari Crater, Tongariro Volcano, New Zealand. The eruption produced a range of volcanic hazards including ashfall (as far away as Napier, ~110 km from the vents), at least three cold surges, a debris avalanche and ballistics (Lube et al. 2014; Pardo et al. 2014; Procter et al. in press). Ballistics and surges were considered to be the main threats to life produced in the eruption, with ballistics impacting a ~6 km^2 area which included 2.6 km of the Tongariro Alpine Crossing (TAC), hiked by ~80,000 people each year, and Ketetahi Hut. It was the first eruption to occur from Upper Te Maari since 1899 (Scott and Potter 2014) and was followed by a smaller eruption on 21 November, 2012. This eruption is thought to have ejected ballistics, but were not ejected far enough to pose a risk to the TAC. There was concern that these events might have been the beginning of a prolonged episode, similar to the 1896 - 97 eruption episode, which would create an ongoing ballistic and surge hazard to the TAC (see Jolly and Taig 2013). Ballistic hazard and risk assessments were completed prior to re-opening of the TAC to the public, however, due to the risk of further eruption and the need for timely assessments, these were based on very preliminary field mapping data with

impact densities from a single area of interest (Ketetahi Hut) used to estimate hiker vulnerability for the entire affected track (from the August eruption; Jolly and Taig 2012; 2013).

This study aims to produce a detailed assessment of ballistic hazard and risk from Upper Te Maari Crater. This will be achieved through:

1) A review of mapped ballistic distributions at other volcanoes around the world.
2) A review of the eruptive history of Upper Te Maari and its eruptive styles and frequencies.
3) Field and orthophoto mapping of the 6 August, 2012 ballistic impact crater distribution.
4) Calibration of the Tsunematsu et al. (2013) ballistic trajectory model using the 6 August ballistic impact distribution, and refinement of eruption parameters through inverse modelling.
5) Forward modelling of three possible future eruption scenarios using the calibrated Tsunematsu model.
6) Vulnerability analyses along the Tongariro Alpine Crossing, incorporating variations in ballistic impact density along the impacted track.

1.2 RISK MANAGEMENT FRAMEWORK

The risk management framework, produced by the International Standards Organisation (ISO), was used as a conceptual framing of this thesis. This framework provides different research organisations and research groups with a common guideline to risk reduction through a process of risk identification, analysis, evaluation and treatment (Figure 1; ISO 2009). Following the Upper Te Maari eruptions, GNS Science utilised this framework to produce risk assessments, as such, the framework is outlined to show how this study contributes to managing the hazard and vulnerability associated with volcanic ballistic projectiles ejected from Upper Te Maari Crater, Tongariro (Jolly and Taig 2012; 2013).

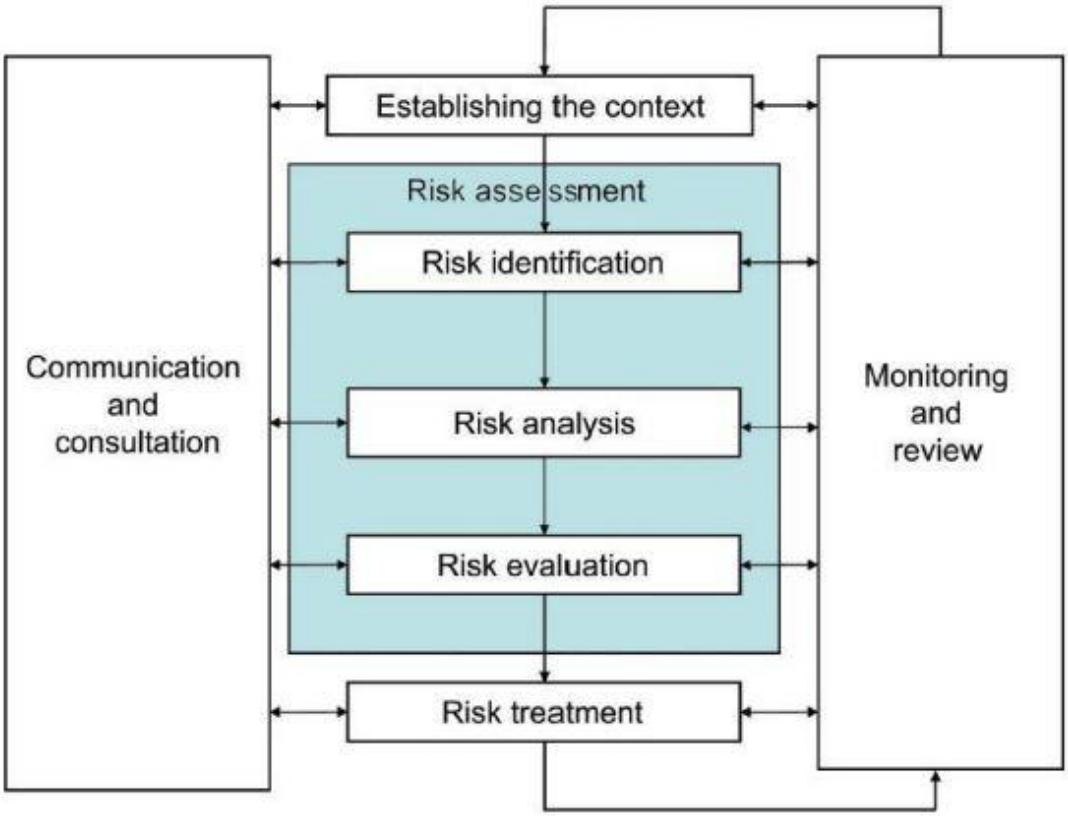

Figure 1. ISO 31 000 risk management framework (ISO 2009).

Risk is a product of hazard and vulnerability and is expressed in the equation:

Hazard x Vulnerability = Risk

Hazard is defined as a natural event (such as a volcanic eruption) that has the potential to cause harm or loss of life and damage to buildings, infrastructure and the environment. The probability of occurrence of the event within a specific time period and a given area, and the magnitude of the event are also incorporated (Marker 2013; Nadim 2013). The term vulnerability refers to the degree to which a person, buildings or infrastructure is likely to experience harm, loss or damage from exposure to the hazard (Cutter 2013). Risk refers to the probability that harm, loss or damage will occur as a result of the hazard.

The first step in the risk management process is to establish the context, including the scope and objectives, of the study. This is followed by risk identification in which all potential

volcanic hazards within a specific area are identified and their impacts characterised. This step also includes identifying all elements (i.e. people, infrastructure, buildings) that are at risk from the hazard and how they relate spatially and temporally with the hazard, and their potential vulnerabilities (Crozier and Glade 2005). In volcanic risk assessment, hazard maps are a primary communication tool used to portray this information to decision makers, the public and other scientists (Sparks et al. 2013; Appendix A). Hazards are identified through review of previous events that have occurred in the area of interest from geologic and literature investigations (Tilling 1989; Blong 1996; Sparks et al. 2013). Essentially, this step identifies all factors that require further investigation in the risk analysis step (Crozier and Glade 2005). In this study, based on the 2012 Te Maari eruptions, ballistics were identified as a considerable ongoing hazard and hikers along the Tongariro Alpine Crossing as elements that may be impacted, requiring further analysis.

The risk analysis and evaluation steps focus on developing an understanding of the identified risks, in order for them to be compared and prioritised (ISO 2009). This involves assessments of the frequency and magnitude of the volcanic hazards and the vulnerabilities of the exposed elements. The assessments can be deterministic, probabilistic or a combination of both. Deterministic assessments use hypothetical eruption scenarios based on previous eruption data (typically the maximum credible events) to determine the impact of volcanic hazards on the elements. However, several limitations are evident including: uncertainty of risks due to subjective judgements by experts; scenarios can only be assessed one at a time; and the likelihood of the risks are not quantified (Kaye 2008). For this reason probabilistic assessments are increasingly desired. Probabilistic assessments are used to determine the probability of a hazard occurring and its associated damage from a range of scenarios (varying in magnitude and frequency), with limited subjective input. The degree of damage in each scenario can be determined by incorporating fragility functions into the probabilistic risk assessment. Vulnerability or fragility functions are probabilistic functions which relate the amount of damage to an element, or vulnerability, to hazard intensity (e.g. ashfall thickness, ballistic impact density). They are helpful during risk assessment as it can be seen under which conditions damage or disruption can occur and where mitigation measures may help reduce damage and risk. This information can also be presented in a hazards map to illustrate levels of hazard and risk around a volcano. A combination of

deterministic and probabilistic methods are used in this study to assess ballistic hazard and vulnerability from Upper Te Maari. Eruption frequency and magnitude are determined from the eruptive history of Upper Te Maari and a frequency-magnitude split used to estimate probabilities of occurrence for three eruption sizes (probabilistic). These scenarios are then modelled using a 3D ballistic trajectory model in order to analyse and compare hazard and vulnerability in possible future scenarios (semi-quantitative deterministic).

Risk treatment, the final step in the risk management framework, is aimed at reducing the hazard and/or vulnerability of the elements within the affected area. Reduction of volcanic hazards in most cases is difficult and sometimes impossible as they are natural events that are not easily controlled (Blong 1996). Thus, it is more beneficial to focus on reducing the vulnerability rather than the hazard. Vulnerability can be reduced through: implementation of various mitigation strategies/actions/techniques developed through the integration of laboratory and field analysis; volcanic surveillance that may indicate volcanic unrest, leading to closures and evacuations; and education and communication with the public about the volcanic hazards and risks they may face and how they can reduce their personal vulnerability (Blong 1996; Tilling 2008). Vulnerability reduction at Upper Te Maari is ongoing. The hazard maps and analysis initiated in this thesis are presented to facilitate and promote vulnerability reduction at Upper Te Maari and other volcanoes worldwide.

1.3 OUTLINES OF THESIS STRUCTURE/RESEARCH METHODOLOGY

Chapter 1 provides an introduction to ballistic hazard, hazard and risk assessments and an overview of the risk management framework as a conceptual framework for this thesis. Chapter 2 is focussed on risk identification through a literature review on the geological setting, eruptive history of Te Maari and its eruptive frequency, ballistic impacts, ballistic distribution maps and ballistic models. Chapter 3 describes the field study on the 6 August 2012 eruption ballistic distribution, results from the calibration of the ballistic trajectory model to the field results, and hazard assessments on this and two possible future eruption scenarios. Risk analysis and evaluation were completed through determination of vulnerability along the Tongariro Alpine Crossing (TAC) to a person at the time of exposure, for the three eruption scenarios. This was achieved through ascertaining the area of hazard

produced by a ballistic and the impact density from each scenario. Chapter 4 describes limitations of the study and opportunities for future work. Conclusions are drawn in Chapter 5.

Chapter 3 is a journal article which has been accepted and is in press as part of the Journal of Volcanology and Geothermal Research Special Issue: Tongariro Volcano. For this paper, I completed the vast majority of field mapping, orthophoto mapping and data analysis, as well as writing the vast majority of the paper. Collaboration with co-authors was required as part of data collection and manuscript preparation, which I outline here:

- Ben Kennedy (senior supervisor; UC), Tom Wilson (co-supervisor; UC), Art Jolly (associate supervisor; GNS Science) and Gert Lube (associate supervisor; Massey University) provided discussion on data analysis and interpretation and conceptual development of the research as part of normal academic supervisory relationship.
- Kae Tsunematsu, Mount Fuji Research Institute, collaborator. Kae ran the ballistic trajectory model from her computer in Japan, though using my field data and with me leading the source parameter selection and completing analysis.
- Eric Breard, Massey University, collaborator. Eric provided additional data (~20 crater locations) collected that outlined the edge of the ballistic field to the east and south, outside the orthophoto extent and which I was not able to reach in the field
- Jo Pawson, University of Canterbury, collaborator. Field assistant - mapping.
- Michael Rosenberg, GNS Science, collaborator. Provided block data GNS collected near the crater and around Ketetahi Hut in the days immediately following the eruption).
- Shane Cronin, Massey University, collaborator. Provided discussion on data analysis and interpretation.

CHAPTER 2: LITERATURE REVIEW

2.1 INTRODUCTION

A literature review was conducted to address the thesis research aims and objectives by: understanding the geology of the study area; assessing Upper Te Maari's eruption history to understand eruptive style and the frequency of eruptions; identifying impacts to people and buildings from ballistic strike; reviewing published ballistic distribution maps in relation to fully identifying hazards; and reviewing the progression of models of ballistic trajectory to introduce the model used in this study.

2.2 GEOLOGICAL SETTING

2.2.1 TAUPO VOLCANIC ZONE (TVZ)

The boundary between the Pacific and Indo-Australian plates controls much of New Zealand's current geology. In the northern part of New Zealand subduction of the oceanic Pacific Plate beneath the North Island (continental Indo-Australian Plate) occurs obliquely at a rate of 42 – 50 mm/yr. (Cole 1990; De Mets et al. 1994; Bibby et al. 1995). This is expressed by the Taupo-Hikurangi arc-trench system, contiguous with the northern Tonga-Kermadec arc system, extending from the Hikurangi Trough east of the North Island to the Taupo Volcanic Zone at the western edge of the system (Carter 1980; Cole and Lewis 1981; Cole 1990). The Taupo Volcanic Zone (TVZ) denotes the currently active arc and back-arc basin and the location of active volcanism from the Late Pliocene (~2 Ma) to the Quaternary (Cole 1990; Wilson et al. 1995). The TVZ stretches from Ohakune to the edge of the continental shelf (~100 km offshore), some 300 km in length and at its maximum 60 km in width, in a NNE - SSW trend (Cole 1990; Wilson et al. 1995). Extension rates vary along the TVZ due to the oblique subduction and subsequent clock-wise rotation of the forearc, with ~15 mm/yr occurring at the Bay of Plenty decreasing to <5 mm/yr close to the southern termination (Wallace et al. 2004; Reyners 2010).

Volcanic composition in the TVZ ranges from basalt to rhyolite. However, andesitic volcanism and stratovolcanoes are dominant in the southern (Tongariro Volcanic Centre) and northern (Bay of Plenty) sections, while rhyolitic volcanism and calderas occur predominantly in the central section (Graham et al. 1995). Spinks et al. (2005) proposes that

the northern and southern sections have more dextral shear and smaller eruptive volumes compared with the central section which has greater eruptive volumes and is purely extensional.

2.2.2 TONGARIRO VOLCANIC CENTRE (TgVC)

The Tongariro Volcanic Centre (TgVC), located at the southern tip of the TVZ, is comprised of four large volcanoes (Tongariro, Ruapehu, Pihanga and Kakaramea), three smaller centres (Pukeonake, Mangakatote and Hauhungatahi) and four craters near Ohakune (Cole 1986; 1990; Figure 2A). Eruptive products of the TgVC are predominantly calc-alkaline medium K andesites with minor occurrences of basalt and dacite (Cole et al. 1986; Graham and Hackett 1987). Based on the compositional variation in lava flows and pyroclastic units, Gamble et al. (1999), Hobden et al. (1999), Price et al. (2005) and Kilgour et al. (2013) propose that magma in the TgVC is erupted from a complex system of multiple small holding chambers, such as dikes and sills, in the crust and upper mantle rather than larger crustal magma reservoirs.

Pebbles of Mt. Ruapehu andesite found in Lower Pleistocene conglomerates indicate volcanism at the TgVC has occurred for at least 300 ka (Fleming 1953). Many of the older vents of the TgVC (Kakaramea and Pihanga) are aligned in a SE orientation, differing from the younger post 20 ka vents that are oriented NNE – SSW (Cole et al. 1986; Graham and Hackett 1987). The younger vent lineation parallels the trend of the Taupo Fault Belt, a dense system of normal faults that accommodate the extension in the back-arc basin, and the present day subduction system (Graham and Hackett 1987; Berryman and Villamor 1999).

Tongariro Volcano, the second largest volcanic edifice (c. 60 km^3) in the TgVC, is comprised of at least 17 overlapping composite volcanic cones, the youngest being Ngauruhoe (Cole et al. 1986; Hobden et al. 1999). K – Ar age determination by Hobden et al. (1996) indicates that Tongariro Volcano has been active for at least 275 ka, with the oldest units found at Tama Lakes. Main periods of cone growth were found to have occurred between 210 and 200 ka, 130 and 70 ka, and 25 ka to the present day. Topping (1974) and Cole and Nairn (1975) divide the Tongariro lavas into older (>20 ka) and younger (<20 ka) episodes. Little

original topographic expression is left of the older lavas, inferred to have erupted from the NW – SE oriented line of vents. The younger lavas erupted from the NNE – SSW trending line of vents including North Crater, Blue Lake, Tama Lakes, Ngauruhoe, Red Crater and Te Maari (Cole 1978; Figure 2B). The latter three vents have also been the location of the most recent activity.

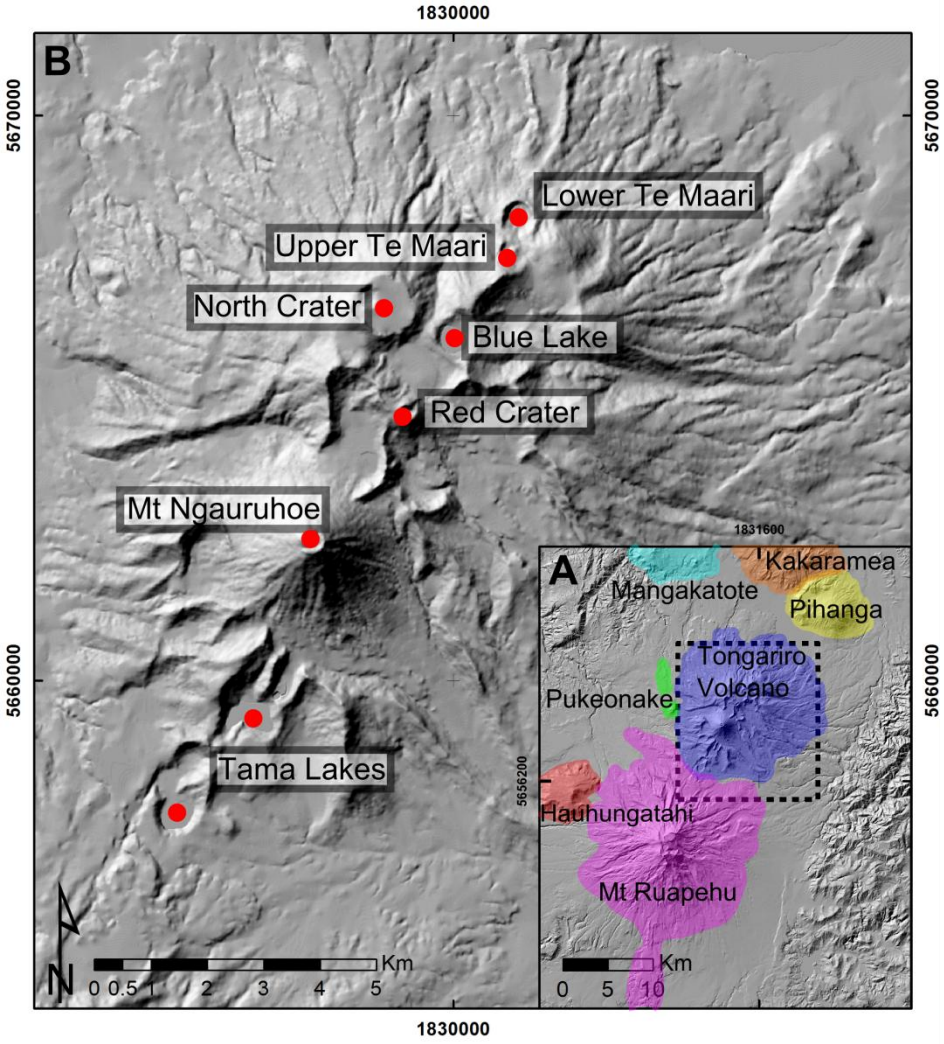

Figure 2. Location map of A: volcanoes comprising Tongariro Volcanic Centre (TgVC) and B: young eruptive vents trending NNE – SSW (DEM is NZSoSDEM v1.0 09 Taumarunui 15 m).

2.3 TE MAARI ERUPTION HISTORY

The Te Maari craters, located on the NE flank of Tongariro, include Upper Te Maari crater (200 m in diameter), Lower Te Maari crater (400 – 500 m wide and 60 – 80 m deep circular crater) and a series of seven small explosion craters northeast of Lower Te Maari (Moebis

2010). Age dating of deposits in and around Te Maari suggests that the area may have been active for hundreds to thousands of years. Eruptions from Te Maari have ranged from rare Plinian events (~10 ka eruptions) to the more common and smaller hydrothermal events (summarised in Table 1). These have occurred both individually and as eruption episodes (1896 – 1897 and 2012). Ballistics were noted in only 3 of the 22 historical eruptions (the 15 December, 1896 eruption, the 6 August, 2012 eruption studied in this thesis and the 21 November, 2012 event), however may have been produced but gone unnoticed or unrecorded in more due to the remoteness of the location 100 years ago. Using all possible historical eruptions (22) over the 145 year eruption history, results in an average eruption frequency of 0.15 per year. However, the majority of the eruptions are grouped together in three periods of heightened activity (1869, 1892 – 1899, and 2012) over 145 years. The annual frequency of occurrence of a period of heightened activity during a period of dormancy is then 0.02 per year. The 2012 eruptions could be considered to be the beginning of a period of heightened activity that may still be ongoing, indicating the probability of eruption may be currently higher than the average frequency over 145 years. An average frequency of occurrence can be found using the 1892 – 1899 period of heightened activity in which 19 eruptions occurred over seven years, indicating an eruption frequency of 2.7 per year.

Nairn et al. (1998) propose Lower Te Maari as a possible source of the Te Rato Lapilli and Poutu Lapilli, tephras of the ~10,000 ka multiple vent Tongariro Plinian eruption episode. Beneath the pyroclastic apron surrounding Upper Te Maari are multiple lava flows extending towards the NW and into Lower Te Maari Crater. Using dendrochronology, Topping (1974) dated the flows as having a maximum age of 1528AD. Local Maori often witnessed eruptions over the past few hundred years from Lower Te Maari (Cowan 1927), however the first written account of activity did not occur until 1839, when Bidwill recorded steam rising from the Northern slopes, likely Lower Te Maari (Gregg 1960).

Accounts of historical eruptions from Upper Te Maari Crater were collated by Scott and Potter (2014) and inform much of the following summary of eruptive activity between 1869 and 1899.

The first eruption from Te Maari recorded in written accounts occurred in early 1869 and is attributed to the formation of Upper Te Maari Crater (Cowan 1927). Hill (1891; 1892) describes an ash column with a “bright red flame” that deposited “dust, pumices and ashes". A further ash-producing eruption was recorded on the 30 November 1892 (New Zealand Herald, 6 December 1892; Gregg 1960; Cole & Nairn 1975). The latter produced a 900 m high column consisting of ash and pumice lapilli, and pyroclastic density currents (PDCs) that reached SH46 around 3 km from the vent (Hill 1893). Pardo et al. (2014) propose that the eruption was hydrothermal or phreatomagmatic in nature.

A series of eruptions, or an eruption episode, commenced on 13 November 1896 with two explosive eruptions of ash and lapilli with possible incandescence (Evening Post, 14 November 1896; Otago Daily Times, 24 December 1896). Ash producing eruptions continued intermittently between the 24 November and the 1 December with larger eruptions on the 27 and 30 November (New Zealand Herald, 1 December 1896; Otago Daily Times, 24 December 1896). Samples of ash collected on the 29 November were very fine grained, suggesting the 27 November eruption may have been phreatomagmatic (Scott and Potter 2014). A few weeks later on the 15 December 1896, Upper Te Maari erupted again though more explosively than any of the previous eruptions in this episode. The eruption produced a >6 km high ash plume, which had a dark red glow at the base, depositing ash as far away as Napier. Incandescent blocks and bombs weighing up to 4 tonnes were ejected as far as 800 m from the vent and a 33 m wide rift was produced upslope. Deposits of “mud, stones and sand” produced in the eruption were found to extend to Ketetahi and Red Crater (Poverty Bay Herald, 16 December 1896; New Zealand Herald, 5 January 1897; Bay of Plenty Times, 13 January 1897; The Press, 16 January 1897; Friedlaender 1898). Pardo et al. (2014) propose that the “mud, stones and sand” may be surge deposits and that the eruption may be comparable to a Vulcanian style with the production of surges, incandescent ballistics and extensive ashfall. Ash eruptions were witnessed again on the 21 December 1896, 25 January 1897 and 6 February 1897, with the latter said to be the largest plume witnessed in this sequence (Auckland Star, 21 December 1896; New Zealand Herald, 26 January 1897 & 28 January 1897; Evening Post, 8 February 1897; Bay of Plenty Times, 12 February 1897). The final three eruptions in this sequence occurred on the 17 and 22 September and 18 October 1897. The 22 September eruption consisted of steam and ash, however the nature

of the earlier and latter eruptions are not known (Poverty Bay Herald, 18 September 1897; Colonist, 21 October 1897). Eruptive activity occurred again at Upper Te Maari between 29 and 30 August 1899 producing an ash plume (New Zealand Herald, 6 September 1899).

An increase in seismicity beneath the northern slopes of Tongariro was noted by GNS Science from the 12 July 2012 (Jolly et. al. 2014). Sampling of fumaroles near Upper Te Maari commencing on the 21 July 2012 also revealed an increase in magmatic signatures (Christenson et al. 2013). This unrest preceded a hydrothermal eruption from Upper Te Maari Crater on the 6 August 2012 at 11:52pm NZST (Rosenberg 2012). The eruption generated a debris avalanche, ~8 km high ash plume, multiple surges and ballistic blocks that travelled up to 2.3 km from vent (Crouch et al. 2014; Lube et al. 2014; Procter et al. in press). A more detailed description is provided in Chapter 3.

Three months after the August eruption on 21 November 2012, a second smaller event occurred. This eruption happened during the day (1:25pm NZST) and was both recorded on monitoring webcams and observed by hikers along the Tongariro Alpine Crossing (TAC). An ash column (3 – 4 km in height) and two small low density pyroclastic flows were generated though did not travel more than a few hundred metres. Finger jets can be seen in videos of the eruption, likely carrying ballistics, however there is no evidence to show them travelling far from the vents (Scott and Fournier 2012a; Scott and Fournier 2012b).

Table 1. Historical eruptions of Upper Te Maari (modified from Scott and Potter 2014)

Date	Description of activity	References
Early 1869	Ash eruption, probable formation of Upper Te Maari Crater, Possible Strombolian eruption ("bright red flame in ash cloud, would burst at top of ash cloud and fall in little pieces like snow")	Hill 1891 & 1892; Cowan 1927; Cole and Nairn 1975
30 Nov. 1892	Ash eruption ~900m in height, accompanied by PDCs	New Zealand Herald (6 December 1892); Cole and Nairn 1975
13 Nov. 1896	2 explosive ash-lapilli eruptions	Evening Post (14 November 1896); Otago Daily Times (24 December 1896)
24 Nov. 1896	Explosive ash eruption	New Zealand Herald (25 November 1896); Otago Daily Times (28 November 1896)
25 - 30 Nov. 1896	Ash eruptions on most days (6 in total), larger eruptions on the 27th (possibly phreatomagmatic due to fine grained ash) and 30th.	New Zealand Herald (1 December 1896); Otago Daily Times (24 December 1896); New Zealand Herald (1 December 1896)
1 Dec. 1896	Ash eruptions continued, brown ash component	Evening Post (1 December 1896); Friedlaender 1898
15 Dec. 1896	Explosive Vulcanian eruption >6 km in height, 15 minutes long, ash column with dark red glow at base, ejected incandescent blocks/bombs, extensive fine and pumiceous ash fall as far as Napier, possible surges	Poverty Bay Herald (16 December 1896); The Press (16 January 1897); Friedlaender 1898; Pardo et al.2014
21 Dec. 1896	Ash eruption	Auckland Star (21 December 1896)
25 Jan. 1897	Ash eruption	New Zealand Herald (26 & 28 January 1897)
6 Feb. 1897	Ash eruption, largest seen in eruptive sequence	Bay of Plenty Times (12 February 1897)
17 Sept. 1897	Eruption (no information on whether steam or ash)	Poverty Bay Herald (18 September 1897)
22 Sept. 1897	Eruption of steam and "smoke"	NZ Herald (23 September 1897)
18 Oct. 1897	Eruption (no information on whether steam or ash)	Colonist (21 October 1897)
29-30 Aug. 1899	Ash eruption	New Zealand Herald, 6 September 1899
6 Aug. 2012	Magmatic hydrothermal eruption. Produced 8 km ash column, debris avalanche, ballistics up to 2.3 km, and at least 3 PDCs	Rosenberg 2012; Crouch et al.2014; Lube et al.2014; Procter et al. in press
21 Nov. 2012	Eruption producing ash column and PDCs	Scott and Fournier 2012a

2.4 BALLISTIC HAZARD IMPACTS

Volcanic ballistic projectiles constitute a major proximal hazard to people, infrastructure and the surrounding environment. Particles range from centimetres to metres in diameter and may be juvenile (bombs) or lithic (blocks) in nature (Steinberg and Lorenz 1983; Yamagishi and Feebrey 1994; Bower and Woods 1996; Alatorre-Ibargüengoitia et al. 2012). They can travel up to ~10 km from the vent (Steinberg and Lorenz 1983; Alatorre-Ibargüengoitia et al. 2012) at up to hundreds of metres per second (Minakami 1942; Nairn and Self 1978; Fagents and Wilson 1993).

Figure 3. Damage to Ketetahi Hut from ballistics ejected in the 6 August, 2012 Upper Te Maari eruption. The ballistic penetrated the roof (A), passing through two bunk beds (B) before puncturing through the floor (photo credit: Emma Rhodes).

Projectiles have high kinetic and impact energies, capable of penetrating buildings and causing serious injury or death to those they strike (Figure 3). Alatorre-Ibargüengoitia et al. (2012) estimate the kinetic energy of projectiles from VEI 2 – 4 eruptions to be ~10^6 J – far greater than the energy needed (400 – 1000 J) to penetrate a metal sheet roof (Jenkins et al. 2014). Ballistics ejected in the 2010 eruption of Pacaya Volcano, Guatemala punched through metal sheet roofs and additionally ignited some of the impacted dwellings (due to

the high thermal energy) ~3 km from the vent (Wardman et al. 2012; Jenkins et al. 2014). Fires were also started by ballistics during the 1994 – 1998 eruptions of Popocatépetl (Delgado-Granados et al. 2001) and the 1999 – 2001 eruption at Colima (Zobin et al. 2002).

Blong (1984) describes accounts of both injury and death as a result of ballistic strike from volcanic eruptions. Three children suffered from fractured skulls in the 1902 Soufriere St Vincent eruption, and one victim had his thoracic cavity pierced and collar bone broken in the June 1914 eruption of Mt Lassen. In the March 1944 eruption of Vesuvius three fatalities occurred from falling bombs up to 5 km from the vent. Five people died and seven were seriously injured from ballistics in the 14 January 1993 eruption of Galeras Volcano, Colombia (Baxter and Gresham 1997). Injuries included skull, jaw, temporal bone, hand and leg fractures, burns, concussion, and lacerations and contusions. Kinetic energies >80 J are suggested by Baxter and Gresham (1997) to be the threshold of lethality of ballistics. They propose a particle weighing 10 kg carries a 90 % probability of death travelling at 6 – 13 m/s. Ballistic velocities are generally much faster than this, thus presenting a high level of hazard and vulnerability to people. However, the probability that a person is hit by a ballistic is dependent on the distribution and impact density around a volcano.

2.5 BALLISTIC IMPACT DISTRIBUTION MAPS

Ballistic impact distribution maps are used to identify the nature and extent (e.g. size and shape of the ballistic field and the variation of impact density) of the ballistic hazard. Published maps are not common and, when they are published, are often incomplete (either only displaying the outer edges of the field or only portions of the field) (Minakami 1942; Nairn and Self 1978; Self et al. 1980; Yamagishi and Feebrey 1994; Robertson et al. 1998; Houghton et al. 2011). This is due to a multitude of reasons including: the risk of further eruption; subsequent deposition of ash or precipitation obscuring craters; the time consuming and labour intensive nature of field mapping; and when mapping can be done remotely (e.g. aerial photos, video, thermal imagery) is hampered by resolution. Maps can include locations of ballistic particles, impact craters when ballistics are not easily found, or a combination of the two. Impact maps can be used to understand eruption dynamics such

as direction, angle and velocity, and can indicate size of eruption (how far ballistics travelled). They are important constituents of volcanic hazard maps.

Complete maps have been produced by Pistolesi et al. (2008) and Gurioli et al. (2013). A combination of field surveys and aerial photos were used by Pistolesi et al. (2008) to map the impact field produced by the 5 April 2003 eruption of Stromboli. Both crater and blocks were located, though blocks <2 m in diameter were not visible on the aerial photos. An asymmetric distribution around the vent was noted, with two concentrated narrow zones to the NE and WSW. Blocks travelled up to ~2 km from the vents and were up to 3.5 m in diameter. Gurioli et al. (2013) also used a combination of aerial photos and fieldwork, though with the addition of thermal imagery, to map a complete Strombolian bomb field produced in the 21 January 2010 eruption of Stromboli. This was possible due to the different dispersal direction from other major eruptions. The SSE – SW directed field consisted of 780 bombs between 7 and 459 cm in diameter that travelled up to 429 m from the vent. Impact density was calculated and ranged up to 100 x 10^{-3} m^2.

More commonly the distribution maps that are produced are incomplete, with only the outer edges of ballistic fields mapped to ascertain the maximum range. Minakami (1942) mapped the outer edge of the ballistic fields produced by the April 20 1935, April 16 1937 and June 7 1938 Vulcanian eruptions of Asama Volcano. The ballistic fields were found to be distributed asymmetrically around the vent in the latter two eruptions, with particles up to 1 m and 7.5 m in diameter travelling ~3.4 and 4.5 km respectively. The earlier eruption produced a nearly symmetrical strew field extending ~2.8 km from the vent. Nairn and Self (1978) provided a map highlighting the approximate range of ballistic ejecta from the February 1975 Vulcanian eruptions of Ngauruhoe. The map, however, excluded the eastern and southern sides of the volcano (possibly due to accessibility as mapping was completed solely by field surveys) and no individual impact locations were presented. They did state that ejected blocks were up to 27 m in diameter and impact craters up to 2 m in diameter were found as far as 2.8 km from the vent. Yamagishi and Feebrey (1994) and Robertson et al. (1998) also outlined the maximum extent of the ballistic fields from the respective 1988 - 89 Vulcanian Tokachidake (~1 km) and Sub-Plinian 17 September 1996 Soufriere Hills (~2.1

km with impact craters up to 6 m in diameter and blocks up to 1.2 m) eruptions, though do not provide individual impact locations.

The boundary of the ballistic field and 200 blocks and bombs in eight radiating profiles (from the vents) were mapped by Self et al. (1980) from the Ukinrek Maar eruptions in 1977. Two distributions were found: an earlier eruption had ejected blocks 2 – 3 m in diameter up to 700 m from the crater increasing in size with distance; and a later eruption of bombs and blocks that travelled the same distance as the previous distribution but projectiles decreased in size with distance.

Isopleth maps of ballistic fields are presented in Kilgour et al. (2010) and Houghton et al. (2011). Kilgour et al. (2010) mapped the ballistic fallout from the 25 September 2007 Surtseyan eruption of Mt. Ruapehu, though again individual ballistic locations are not presented. A combination of orthophoto analysis and field surveys (though limited due to the risk of further eruption) were used to map the northerly directed strew field in which blocks up to 2 m were ejected up to 2 km from the vent. Ballistic ejecta (<50 cm in diameter) from the 19 March 2008 eruption of Kilauea were mapped by Houghton et al. (2011). However, the ~300 m wide field directed toward the SE could not be mapped in its entirety due to part of the field being located within the crater.

A greater level of detail included in distribution maps creates a greater understanding of the hazard and more accurate hazard maps. Nine of the eleven ballistic fields mapped in these eruptions are asymmetric in shape, indicating that the eruptions were directed. These directions may be preferential in multiple eruptions resulting in directional zones of increased hazard, rather than the simplified concentric zones produced using a maximum travel distance. Complete maps (rather than just field outlines) allow impact density to be calculated – another factor that can define zones of varying hazard. Generally the complete maps utilised more resources including aerial photos, thermal imagery and field work compared with the incomplete maps that relied mainly on fieldwork, likely limited by time constraints and the possibility of further eruptions.

2.6 BALLISTIC MODELS

Ballistic blocks and bombs generated in volcanic eruptions decouple from the eruptive column to follow nearly parabolic trajectories (Minakami 1942; Wilson 1972; Fagents and Wilson 1993). Models of particle transport are valuable tools in both ascertaining eruption dynamics (correlating initial particle velocity with deposition distance) and modelling and assessing ballistic hazard.

To determine the initial velocities of ballistics ejected from eruptions of Asama volcano, Japan, Minakami (1942) created a mathematical expression that related ejection velocity and angle to the distance the ballistic travelled (based on mapping of the outer edges of the impact field), including the effects of drag and wind speed.

The initial velocity of ballistics ejected in the 1968 eruption of Arenal Volcano was estimated using a model derived by Fudali and Melson (1972). In the absence of ballistic size (projectiles broke and scattered on impact), the authors used impact energy derived from crater size and a series of ballistic trajectory calculations to estimate ballistic size and maximum initial velocity. Both this and the previous model assume a spherical ballistic shape to determine their drag coefficient.

The first mathematical algorithm that modelled ballistic trajectories was developed by Wilson (1972). Trajectory was expressed through a rectangular coordinate system and a 4^{th} order Runge-Kutta method, taking into account gravity and drag forces (assuming a cylindrical shape rather than spherical due to its aerodynamic properties) and allowing for changes in atmospheric properties with height. Wilson explored fall times of clasts of varying size and density from various heights, and the ranges of clasts ejected as a function of initial velocity, ejection angle and clast density and size. Steinberg and Lorenz (1983) apply a variation of this model to improve previous particle velocity estimates at Asama (Minakami 1942), Arenal (Fudali and Melson 1972) and Shiveluch Volcanoes.

Calculations and models prior to the 1990s assumed a still, ambient atmosphere into which ballistics were ejected. This resulted in overestimations of drag on particles and

subsequently initial particle velocity. Fagents and Wilson (1993) recognised that the air overlying the vent is displaced en masse in volcanic explosions, at speeds initially comparable to the ejected clasts. Ballistics are essentially coupled initially with the displaced surrounding air, reducing the drag force to nearly zero, until the air and ballistics progressively decouple at which time drag increases. An additional model describing the explosion process is applied prior to the trajectory model devised by Wilson (1972). The ejected material initially behaves as a coherent plug before reaching a maximum velocity, at which the ballistics are then launched into the decelerating gas flow field. Once launched, trajectory is then modelled using the Wilson (1972) model (though drag is now proportional to the square of the ballistic velocity relative to the moving air, rather than the still atmosphere in the original model).

Bower and Woods (1996) followed Wilson (1972) and Fagents and Wilson (1993) in using equations of motion to model ballistic trajectory. Their model differs, however, from Fagents and Wilson in that they model the trajectory of ballistics from small eruptions, ejected from above the crater after separating from the collapsing jet at the crater rim and encountering a still atmosphere. Bower and Woods (1996) propose particles are accelerated when coupled with the jet phase within the conduit and vent until a shockwave is produced as the jet meets the crater, causing the jet to decelerate but the ballistics to decouple and continue with their original velocity.

'Eject!', a computer programme modelling ballistic trajectory, was developed by Mastin (2001) to allow users to model their own scenarios. Following Wilson (1972), trajectory is modelled using a rectangular coordinate system and a Runge-Kutta method. Users can define the drag coefficient, ballistic shape, particle density and diameter, atmospheric properties, ejection angle and initial velocity. A function quantifying the zone (distance) of reduced drag around the vent was also added, similar to Fagents and Wilson (1993).

In previous models the drag coefficients used were of geometrical shapes (e.g. sphere, cube and cylinder). Alatorre-Ibargüengoitia & Delgado-Granados (2006) measured the drag coefficients (C_d) of volcanic particles in a subsonic wind tunnel. They found that C_d depended mainly on particle shape and texture and that the lowest C_d values should be

applied in models to calculate maximum possible range. These results were then incorporated into a ballistic trajectory model. Alatorre-Ibargüengoitia et al. (2012) coupled this model with an eruptive model that considered caprock acceleration and consumption of energy during fragmentation, informing ballistic velocity.

The aforementioned ballistic models, and the many others not mentioned, consider movement of particles only in two dimensions and are only capable of modelling individual particles. Tsunematsu et al. (2013) developed a three dimensional model that simulates the trajectory of multiple ballistics and includes the effects of particle collision – something not previously considered. The model is also the first to output the spatial distribution of the ejected ballistics on the ground (assuming a flat surface), allowing direct comparison to impact distribution maps. Trajectories are modelled using equations of motion and a discrete event simulation method. Required input parameters include rotation and inclination angle (ejection angle and standard deviation), initial particle velocity, particle density and diameter, ejection direction, displacement of ejection points from the vent centre (spread of ejection points), the number of particles ejected (per burst if more than one eruption burst), and time interval between bursts. The model, originally designed for Strombolian eruptions, is utilised for hydrothermal eruptions in this study, and the effects of drag and the initial coupling of particles and gas jet is also introduced.

CHAPTER 3: RESEARCH COMPONENT

3.1 INTRODUCTION

Chapter 3 contains the new research component of this study in which field and orthophoto mapping of the 6 August ballistic distribution, calibration of the Tsunematsu (2013) model, forward modelling of possible future eruption scenarios and vulnerability analyses along the TAC are presented. It draws on the literature review undertaken in Chapter 2. The chapter is structured in the follow way:

- Detailed overview of the 6 August, 2012 Upper Te Maari eruption.
- Methodology describing how orthophoto and field mapping of the 6 August ballistic distribution were carried out, past ballistic trajectory models and the adopted Tsunematsu et al. (2013) model, and how ballistic vulnerability is calculated.
- Results of both the spatial and crater size distribution from ballistic block impacts of the 6 August 2012 eruption, obtained through a combination of orthophoto mapping and ground truthing. The crater distribution is then combined with acoustic data, observations of vent morphology, and eyewitness accounts of the eruption to parameterise a ballistic trajectory model (Tsunematsu et al. 2013).
- Discussion in which the calibrated model is used to forward model the ballistic hazard from two other possible future eruption scenarios. Ballistic vulnerability along the impacted TAC is then calculated using the method described in the methodology, for the 6 August modelled distribution as well as the two possible future scenarios.
- Conclusion summarising main results.

3.2 OVERVIEW OF 6 AUGUST 2012 ERUPTION OF UPPER TE MAARI

On 6 August 2012 at 23:52 (GMT +12) a small ~19 s hydrothermal eruption occurred at Upper Te Maari, following a collapse and subsequent debris avalanche from the hydrothermally altered western flank of the crater (Jolly et al. 2014, Procter et al. in press). The eruption formed a ~430 m long arcuate fissure, split into a wider (>50 m) and deeper

(~30 m) western section closest to the collapse scarp, and a narrower (>10 m) and shallower (>10 m) eastern side upslope of Upper Te Maari crater. Eyewitness accounts describe three short-lived explosions that produced eruption clouds: the first emanating from the East at an angle <45° (from vertical), followed by a shallower (>45° from vertical) eruption cloud from the West, with a final central eruption producing a vertical ash column (Lube et al. 2014). GeoNet acoustic monitoring data shows five pulses of eruption, each with a duration of 3 - 5 s (Jolly et al. 2014).

Sampling and analysis of the gas geochemistry from nearby fumaroles, taken prior to eruption, indicated an injection of magma at shallow depths, however, analysis of the erupted ash did not indicate the presence of juvenile material (Christenson et al. 2013; Pardo et al. 2014). This suggests that the eruption was caused by flank collapse induced decompression of a pressurized hydrothermal system, likely enhanced by shallow-seated magma (Pardo et al. 2014). Surges were produced from the eastern and western directed explosions, as evidenced by the asymmetric extent of the mapped deposit (Lube et al. 2014). Ballistic blocks were dispersed over a ~6 km^2 area, impacting the Ketetahi Hut and ~2.6 km of the TAC, at its closest 1.2 km from the vents and traversed by ~80,000 people annually. The hut suffered damage, with blocks penetrating the roof and floor. This was the first eruption from Upper Te Maari since 1899 (Scott and Potter 2014) and there was concern that the August event might have been the beginning of a prolonged episode that would create ongoing ballistic hazards on the TAC (Figure 4). Thus, analysis of the ballistic hazard and risk was required prior to the reopening of the track to the public. A smaller subsequent eruption occurred on 21 November 2012, though ballistics are not thought to have travelled further than a few hundred metres from the vents.

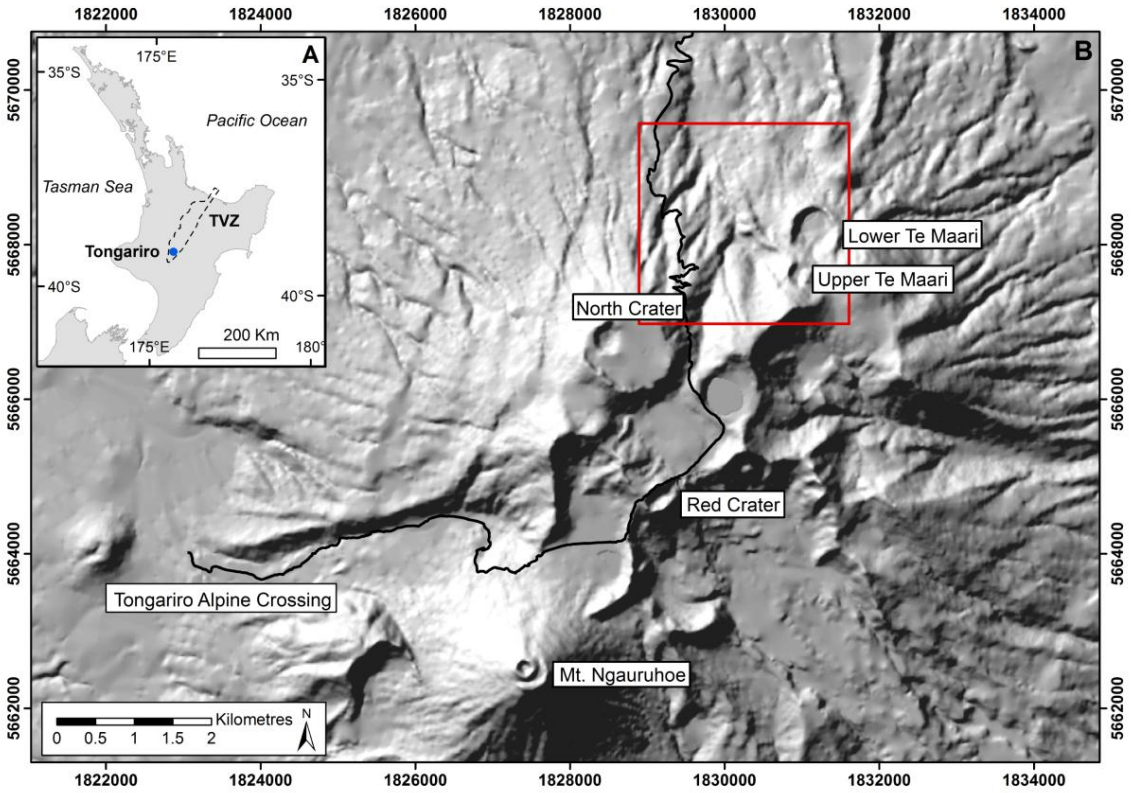

Figure 4. A: Location map of the Tongariro Volcanic Centre within the Taupo Volcanic Zone in the North Island, New Zealand. **B:** Digital Elevation Model (DEM) (NZSoSDEM v.1.0 09 Taumarunui 15 m) of the northern section of Tongariro showing Upper Te Maari Crater and the surrounding craters. Red square indicates study area.

3.3 METHODOLOGY

3.3.1 ORTHOPHOTO MAPPING

An initial study of the distribution of ballistics from the 6 August eruption was performed using high resolution orthophotos (ground-sample distance of 0.2 m), collected on the 8 – 9 November, 2012 (prior to the November eruption). A 100 x 100 m spaced grid was placed over the orthophotos to allow for systematic mapping of impact craters. Identification of impact craters was more difficult where craters were <2 m in diameter due to the resolution limits of the orthophotos.

3.3.2 FIELDWORK

Field campaigns followed the orthophoto mapping to ground-truth the mapped craters and collect data that could not be retrieved from the orthophotos. Fieldwork was conducted in eight locations, chosen at varying distances and azimuths (N, NW and W) from the vents to investigate changes in crater size and density with distance and direction from vent (Figure 5). Surveyed areas were ~10 m in width and up to 160 m in length. However, the extent of the area ground-truthed varied at each location due to time constraints and the impact density in the area. Thus, when the number of impacts mapped by orthophoto were compared with those ground-truthed, standardised 200 m² areas were used to maintain continuity.

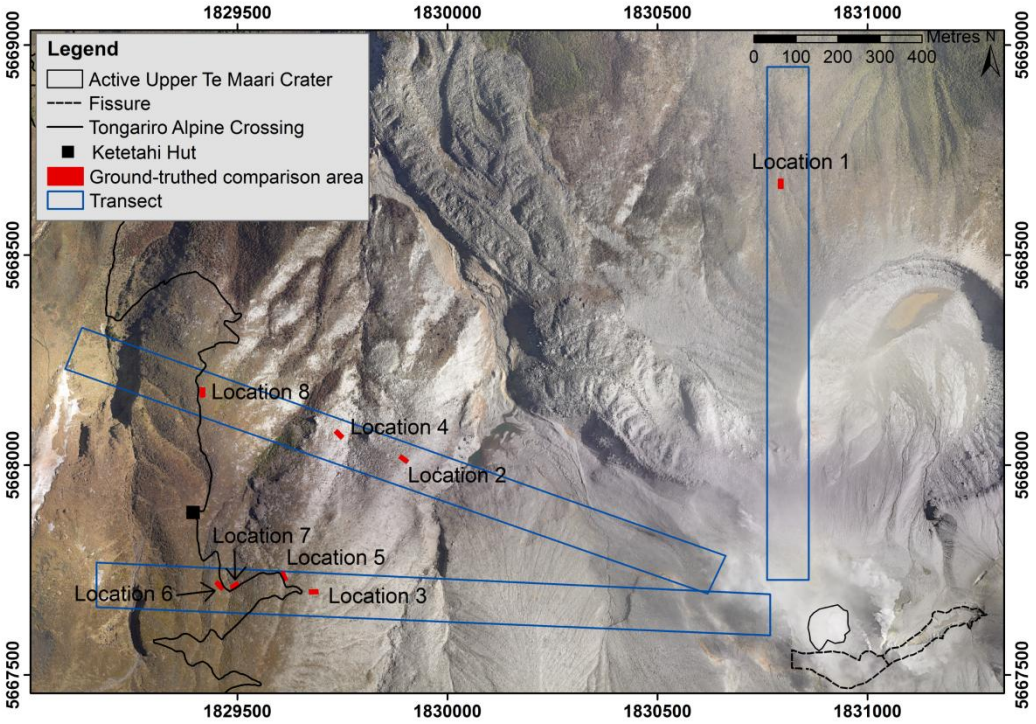

Figure 5. Orthophotos of Upper Te Maari Crater outlining the W, NW and N transects used in data analysis and the 8 locations where fieldwork was conducted (only the impact density comparison areas are shown, though the total area ground truthed is larger). The active Upper Te Maari Crater and fissure are delineated.

At each impact crater, the location was recorded via GPS (NZTM2000), both crater and block (if found) dimensions collected and notes taken on the lithology and degree of alteration of the block. Where possible, the angle of impact (from horizontal) was measured by taking the angle from the middle of the crater to the middle of the block. This measurement could only be taken from narrow, steep-walled 'burrow type' craters in which blocks had remained buried within the crater. As the orthophotos do not fully cover the entire area impacted by ballistics, field surveys were required to find the outermost edge of the ballistic field on the eastern side (Breard et al. 2014).

3.3.3 BALLISTIC TRAJECTORY MODEL

Inverse modelling can use characteristics of the ballistic field to estimate eruption parameters. Many models have been developed to model ballistic trajectory (Minakami 1942; Fudali and Melson 1972; Wilson 1972; Steinberg and Lorenz 1983; Fagents and Wilson 1993; Bower and Woods 1996; Mastin 2001; Alatorre-Ibargüengoitia and Delgado-Granados 2006; Alatorre-Ibargüengoitia et al. 2012) though only consider particles moving in two dimensions and one particle at a time. However, the Tsunematsu et al. (2013) model considers multiple particles in three dimensions, includes the effects of particle collision and computes a two dimensional particle distribution on the ground surface (assuming a flat surface). The output of a particle distribution of all modelled particles allows direct comparison to impact distribution maps, ideal for reverse modelling to obtain eruption parameters. A parameterised and validated model can then be used to investigate future eruption scenarios to produce ballistic hazard and risk maps.

The Tsunematsu et al. (2013) model was adopted in this study and developed further to include the effects of drag on ballistic particles, using a finite difference method to solve the following equation (Alatorre-Ibargüengoitia et al. 2012):

$$\frac{\mathrm{D}v}{\mathrm{D}t} = \frac{\mathrm{A}C_d\rho_a(v-u)|v-u|}{2m} - g \qquad (1)$$

Where, $v = (v_x, v_y, v_z)$ is particle velocity, u is the wind or gas flow velocity, t is time, A is surface area of particle, C_d is the drag coefficient, ρ_a is air density, m is the particle mass, and is the gravitational acceleration.

The drag coefficient (C_d) is set to 0.7. This value was based on the work of Alatorre-Ibarguëngoitia and Delgado-Granados (2006). The majority of particles found in the field were sub-angular and relatively smooth in texture (closest to a C_d of 0.7), with some porous and rough (closest to a C_d of 0.6).

The model required the input of eruption parameters including vent location, number of eruption pulses and particles erupted in each pulse (if multiple pulses), rotation angle (ejection angle of particle; Figure 6), inclination angle (standard deviation of rotation angle; Figure 6), particle density and diameter, initial particle velocity, and displacement of ejection points from the vent centre (spread of point sources at each vent). As each pulse was run separately with its own eruption parameters, no particle interaction occurred between the separate pulses; rather particle collisions only occurred within each pulse.

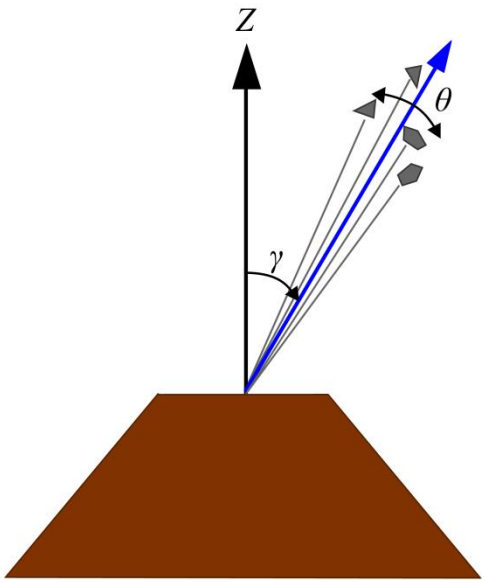

Figure 6. Rotation angle (angle of ejection from vertical (γ)) and inclination angle (standard deviation or variation of rotation angle (ϑ)) model parameters (modified from Tsunematsu et al., 2013).

3.3.4 BALLISTIC VULNERABILITY

The area impacted by a ballistic and the density of impacts over an area can be used to calculate the ballistic vulnerability or probability of casualty (serious injury or fatality) at a certain location. Both the flight path (in which a person would be struck by the ballistic before impact with the ground occurs) and radial impact area (including the block, crater

excavation and debris apron) are combined to ascertain the total area of hazard (Figure 7). The flight path hazard area can be calculated using impact angles measured in the field and the dimensions of a person (taken here as 2 m in height and 1 m in width). Secondly, a radial area of impact is produced by a ballistic. This area of hazard is determined using the crater diameter and width of a person outside the crater to include serious injury or fatality (casualty) within the surrounding ejecta apron. To calculate the length of the hazard posed by the flight path of the ballistic (*L*) the following equation is used:

$$L = 2 / \tan I_a \quad (2)$$

Where I_a is the angle of impact (from horizontal). The area of hazard produced by the ballistic flight path outside of the radial hazard area is found using:

$$A_t = (L - (½\ C + P))\ P \quad (3)$$

Where A_t is the flight path area of hazard (in Figure 7 this is constrained by the width of a person as this is generally greater than the width of a ballistic), *C* is the crater diameter and *P* is the diameter of a person. If *L* < – + *P* then A_t is not applicable as no additional flight path hazard outside of the radial hazard area is produced. Where the block is larger than the diameter of a person, the block diameter (*B*) is substituted for *P* when multiplying the flight path length. The total area of ballistic hazard (A_h) is then:

$$A_h = \pi \left(\frac{1}{2} C + P\right)^2 + A_t \quad (4)$$

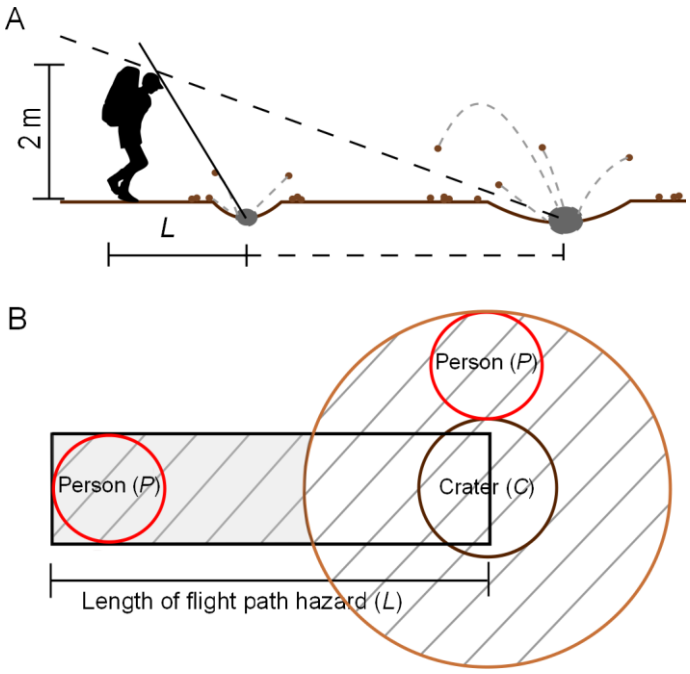

Figure 7. Area of hazard (likely to cause casualty) from a ballistic impact. **A:** Hazard produced from flight path, where the length of the hazardous area increases with shallowing trajectory angles. **B:** Total area of ballistic hazard, combining radial hazard from crater formation and shrapnel production, and flight path hazard. Grey shading indicates additional area of hazard produced by ballistic flight path (A_t) and hatching indicates total area of ballistic hazard (A_h).

The crater rather than the block is used in these equations for two reasons: 1) in many cases the block is not found or it fragments on impact and thus its true size is not known or may then be underestimated. This would result in an underestimation of the ballistic hazard area; and 2) the crater provides the best estimate on the area of hazard as it represents a damage zone where casualty is probable, and also encompasses the ballistic itself. The ballistic size does not need to be known (nor the density or substrate condition) to calculate the area of hazard when using the crater to inform this calculation, and can then be calculated when the block cannot be found.

The size of the debris apron or how far the debris or shrapnel travels from the impact crater may also increase the area of hazard. Pistolesi et al. (2008) noted from the 5 April, 2003 eruption of Stromboli that impacts with hard rock surfaces produced centimetre to decimetre sized shrapnel up to tens of metres from the impact. Impact craters 7 m in diameter ejected soil debris and lava fragments up to 28 m and 15 m from the crater,

respectively in the 2011 Shinmoedake eruption (Maeno et al. 2013). However, debris aprons measured in the field were, on average, 110% greater in size than the crater diameter and blocks generally impacted soil and vegetation (Figure 8). Further work is needed to determine whether impact by shrapnel would cause fatality, or only injure those in the vicinity (and the extent of injuries that would occur).

Impact density is also needed to calculate ballistic vulnerability. The area of ballistic impact hazard was then divided by the impact density from Arc Map (using the Kernel density function) to calculate ballistic vulnerability along the TAC for each eruption scenario.

3.4 RESULTS

3.4.1 SPATIAL DISTRIBUTION OF IMPACT CRATERS

The orthophoto analysis yielded 3,587 craters up to 2.3 km from the vents, with diameters ranging between 0.3 m – 10.8 m (Figure 8 & 9). The ballistic field displays a highly asymmetric shape, reflecting the directed blasts and multiple eruption pulses (Figure 9A). Craters cluster more densely in the WNW ~1,000 m away from the vents, with densities between 2,000 – 6,549 craters/km² (Figure 9B). Clustering on a smaller scale also occurs in the NNE and ESE with densities between 1,000 - 3,000 craters/km². Two areas are noted for their lack of observed impact craters. The first is within ~100 - 200 m of the vent area and the second is on the c.1528AD lava flow.

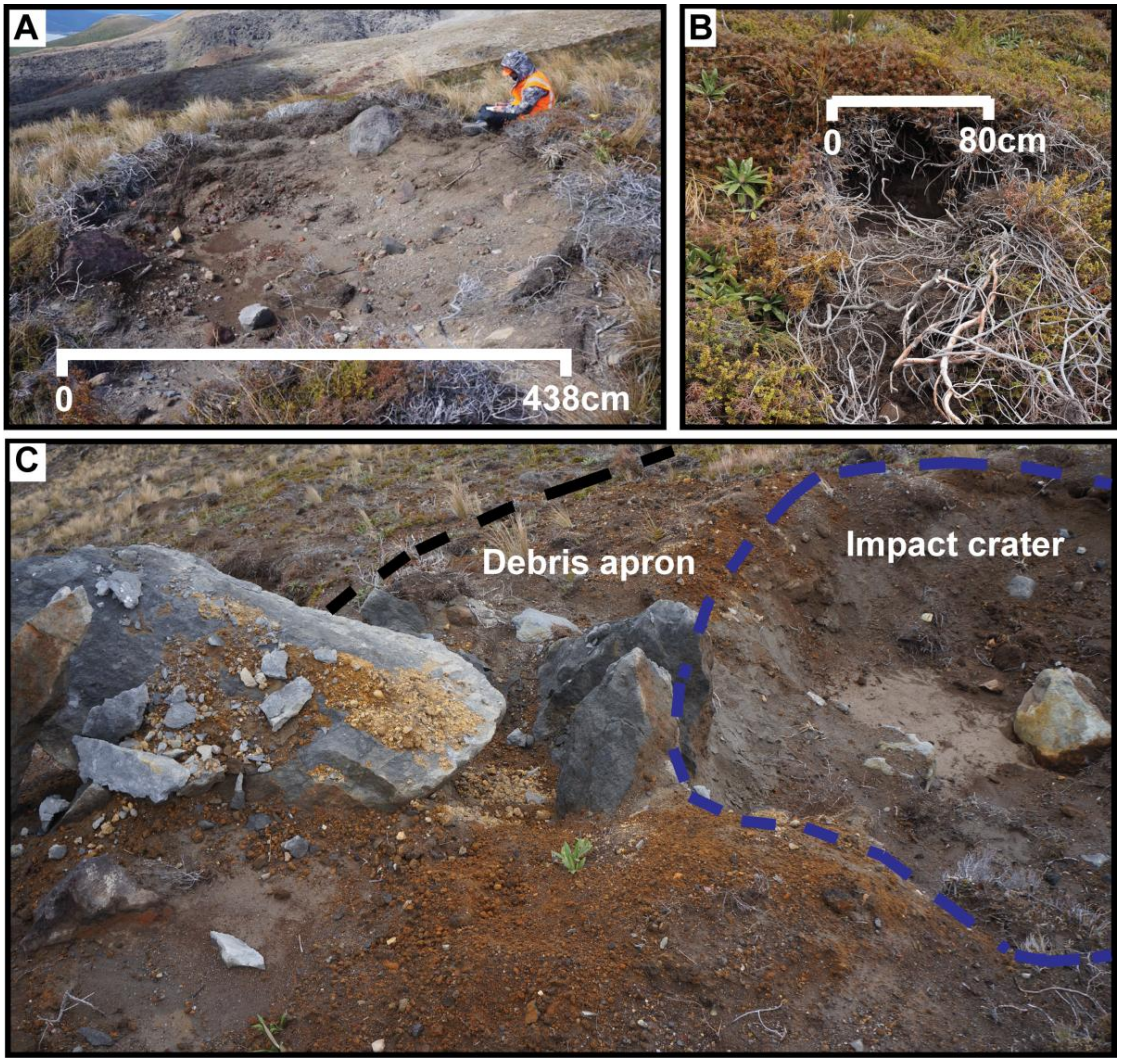

Figure 8. Images of ballistic impact craters highlighting the variation in diameter, impacted substrate and production of debris aprons. **A:** Ballistic fragments within a large symmetrical crater in thinner vegetation. **B:** Smaller more 'burrow-like' crater within thicker vegetation. **C:** Large crater with a debris apron composed of the fragmented block and an orange-brown soil.

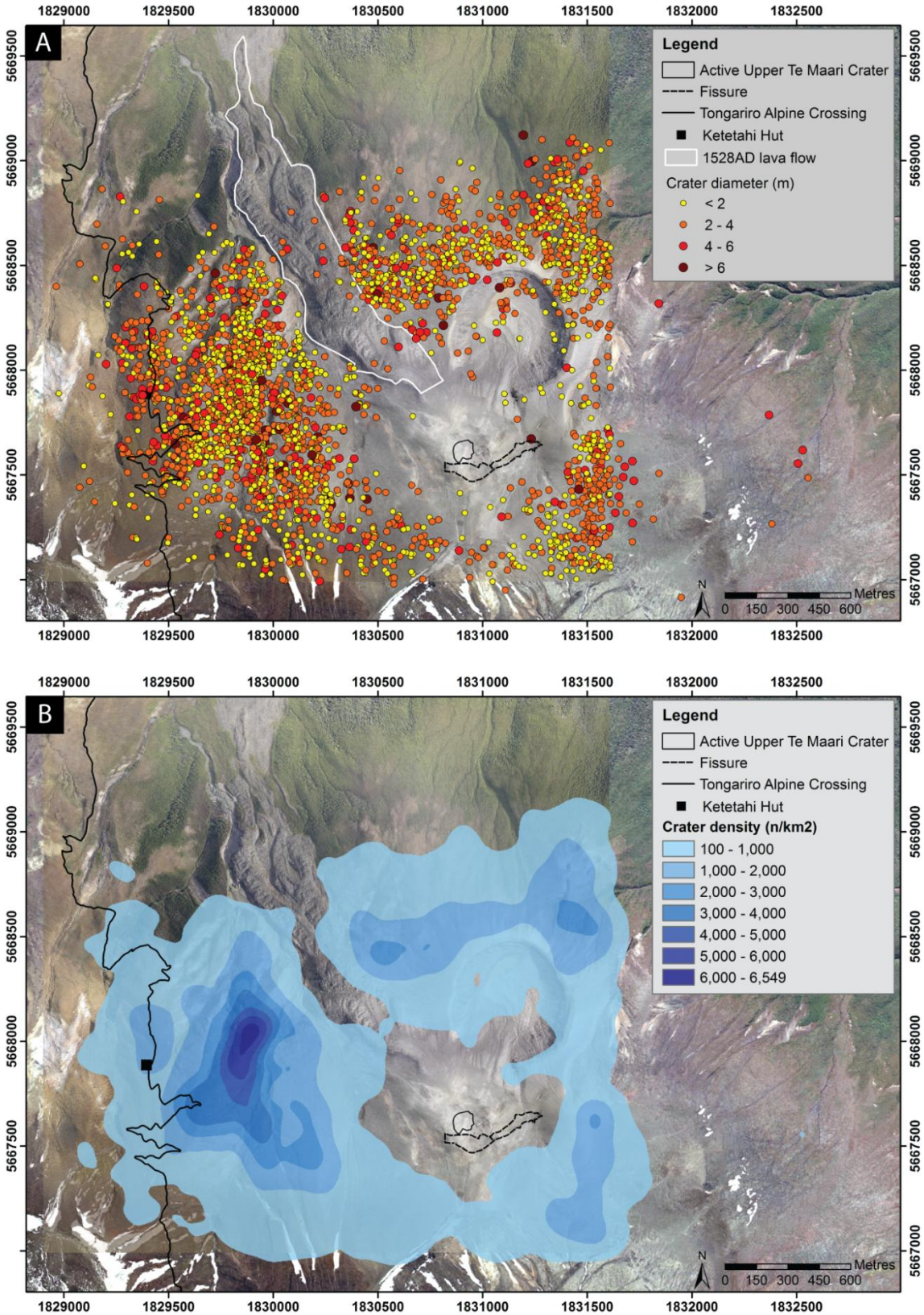

Figure 9. Ballistic impact crater distribution from the August 2012 eruption of Upper Te Maari (see Appendix B (a) for individual crater locations and diameters). **A:** Distribution of craters is delineated by size (mean crater diameter). **B:** Kernel density of craters per km².

3.4.2 Relationship between crater size, distance and direction from the vents and the crater size distribution within the ballistic field

The crater size distribution from the orthophotos was analysed in discrete 750 m wide concentric rings radiating away from the vents (0 – 750 m, 750 – 1500 m, and 1500 – 2250 m). Mean crater sizes of 2.5, 2.3 and 2.7 m were found respectively (Figure 10A). An increase in mean diameter can be seen in the medial to distal rings (750 – 2250 m) showing that there is a general increase in crater size with distance, and therefore larger blocks generally travelled further than smaller blocks (due to the effects of energy and drag – without which ballistic trajectory would be independent of mass). To investigate whether crater size varied at different azimuths around the vents, three transects (towards the N, NW and W) ~100 m wide and spanning the entire ballistic field, were studied from the orthophotos (Figure 5). The W and NW transects have a larger proportion of smaller craters than the N transect with mean diameters of 2.4 m, 2.2 m and 2.7 m respectively (Figure 10B).

Comparing the crater size distribution between the orthophoto mapped and field mapped craters highlights the difference in size and quantity found (Figure 10C). The mean crater size for all orthophoto mapped craters was 2.4 m, compared to a 1.2 m mean for the field mapped craters. Only 19% of the orthophoto mapped craters were <1.5 m in diameter compared to the 74% of field mapped craters.

The number of ground-truthed craters was compared to the number mapped using the orthophotos in a 200 m² area at each ground-truthed location (Figure 5). A large discrepancy is apparent between the number of craters found using the orthophotos (minimum 1, maximum 5) and those mapped in the field (minimum 5, maximum 21). An average ratio of 1 orthophoto crater to 4.5 ground-truthed craters was calculated, indicating that the actual ballistic density may be approximately four times greater than that mapped solely using the orthophotos (Table 2). Since the orthophoto analysis missed many of the small craters and significantly underestimated the true ballistic density, it is clear that a combined orthophoto-fieldwork approach (with higher resolution orthophotos) is needed to avoid significant hazard implications.

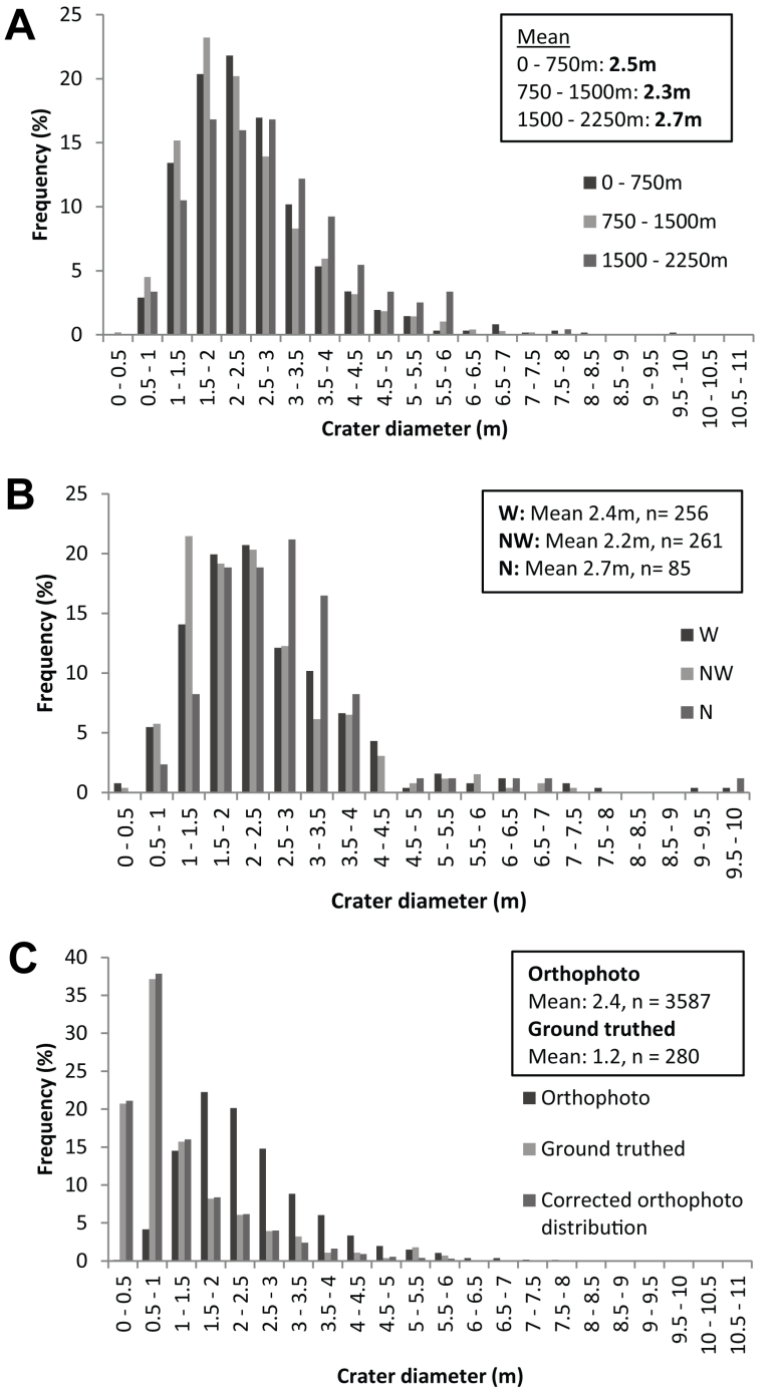

Figure 10. Impact crater size distribution found from orthophoto mapping and ground-truthed data. **A:** Orthophoto impact crater size distribution divided into 750 m concentric rings radiating from the vents. **B:** Orthophoto impact crater size distribution at different azimuths from the vents. **C:** Impact crater size distribution mapped from the orthophotos, from all ground truthed data (see Appendix B (b) for raw fieldwork data), and the corrected distribution combining both orthophoto and ground truthed distributions.

Table 2. Number of impact craters mapped from the orthophotos compared to the number of impacts found when ground truthed, within a 200 m² area at each of the eight ground-truthed locations (selected from larger ground-truthed areas).

Location	Orthophoto	Ground-truthed
Location 1	2	5
Location 2	5	9
Location 3	1	21
Location 4	2	9
Location 5	1	12
Location 6	1	5
Location 7	1	6
Location 8	3	6
Mean	**2**	**9**

3.4.3 Relationship between crater size and block size

Establishing a general relationship between block size and crater dimension is an important tool for approximating the size of blocks ejected in an eruption when only their impact craters can be easily mapped. Crater size is largely controlled by the kinetic energy of the block: a larger block with greater mass has more kinetic energy than a smaller, lighter one when travelling at the same $(KE = \frac{1}{2}mv^2)$ velocity and will therefore create a larger impact crater.

Where possible, measurements of blocks were taken alongside their craters in the field. Only those blocks thought to be whole, and their respective craters, were used. The mean diameter (to allow description of asymmetry) of both the block and crater were calculated and a best fit relationship (a power law with an $r^2 = 0.51$) found showing a general correlation between increasing block size and increasing crater size (Figure 11). This relationship allows for the description of smaller block diameters (<0.25 m) that aren't encompassed in a weaker linear relationship ($r^2 = 0.45$). This method differs from that used by Breard et al. (2014) in that data is combined from all four block lithologies (Defined by Breard et al. as Type 1: dense andesitic lava (d_{avg} = 2.4 g/cm^3); Type 2: andesitic scoria or vesicular lava (d_{avg} = 1.3 g/cm^3); Type 3: breccia, agglomerates and agglutinate blocks (d_{avg} = 2.1 g/cm^3); Type 4: intermediate density columnar jointed andesitic lava (d_{avg} = 2.1 g/cm^3);

all with varying degrees of alteration) to seek a universal relationship regardless of clast density or substrate type. Breard et al. exclusively considered the most common block lithology of Type 1 and generally focussed on larger craters (>2.5 m) to reveal a more defined relationship between block and crater size.

The broader spread of crater diameters in the combined data set is not solely due to the effect of clast density (Type 2 shows a narrower data spread and steeper trend however Type 1, though a broader data set, also shows the same trend with craters <2 m in diameter). It is more likely that the broad data spread is the result of variance in substrate (vegetation thickness and soil strength) and/or from variation in particle velocity (both within a single pulse and also between the multiple pulses) and therefore impact energy. A particle travelling at a faster velocity has more kinetic energy than one, with the same mass, travelling slower and will therefore create a larger impact crater.

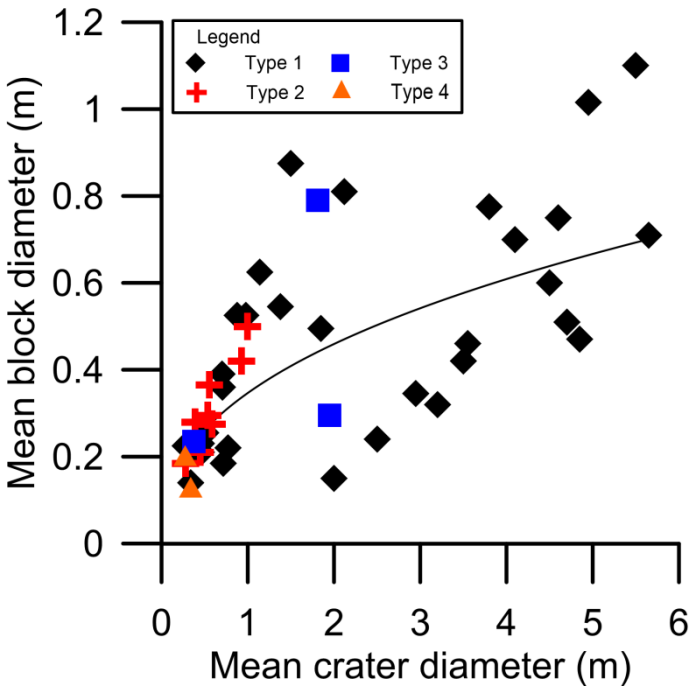

Figure 11. Relationship between block and crater size found in the field (using all lithologies). A power law relationship ($y = 0.3507x^{0.3941}$) was found to be the best fit with a low R^2 value of 0.51.

3.4.4 BALLISTIC TRAJECTORY MODEL

The Tsunematsu et al. (2013) ballistic trajectory model was applied to the results of the orthophoto mapping and field campaigns to evaluate the eruption parameters for the August 6 eruption and to assess the ballistic hazard in future eruption scenarios. To allow for comparison with the field mapped crater distributions, the model particle diameters were converted to crater diameters using the relationship in Figure 11. Many eruption parameters were partially constrained by observations, however in addition, 49 inverse models were then run in order to further constrain some parameters.

3.4.4.1 MODEL PARAMETERS AND RESULTS FOR THE AUGUST 2012 ERUPTION

3.4.4.1.1 NUMBER OF ERUPTION PULSES, VENT LOCATION AND DIRECTION OF PARTICLE DEPOSITION

The vent locations and number of eruption pulses set the initial model conditions. GeoNet acoustic sensors recorded at least five pressure pulses (presumed to indicate the onset of eruption) each with a duration of 3 – 5 seconds (Jolly et al. 2014; Figure 12). The relative eruption energy for each pulse is given by the integral of the pressure differential (ΔP) and the relative energy release of the eruption sequence. Jolly et al. (2014) found that Pulses 1 and 4 each had ~20% of the total energy release of the eruption, while the third pulse included ~50% of the total eruption energy. The two smallest pulses (2 and 5) each released 5% of the total energy.

Consistent with the acoustic sensors, local residents witnessed three major eruption pulses (minor eruptions 2 and 5 were not witnessed) (Lube et al. 2014). They reported that the first occurred to the East at <45° (from vertical), the second to the West at >45° (from vertical), followed by a vertical eruption column. The eastern and western trending surge deposits support the eyewitness accounts, with Lube et al. (2014) attributing the eastern deposit to Pulse 1 and the western deposit to Pulse 3. Stratigraphic logs of the eastern surge deposit revealed a second subunit not belonging to the 1st pulse. Lube et al. (2014) attribute this unit to Pulse 2, with Pulse 4 the vertical cloud seen by eyewitnesses.

The asymmetric shape of the ballistic field and impact crater densities also reflects multiple pulses and directionality of the pulses. Higher crater densities are noted in the W – WNW, N – NNE and ESE. The ESE density is attributed to Pulse 1, NNE to Pulse 2, W – WNW to Pulse 3, and N to Pulse 4 (defining the eruption 'directions' in Table 3). The second pulse must have been directed at a similar angle and eastern direction to be masked by the first larger pulse.

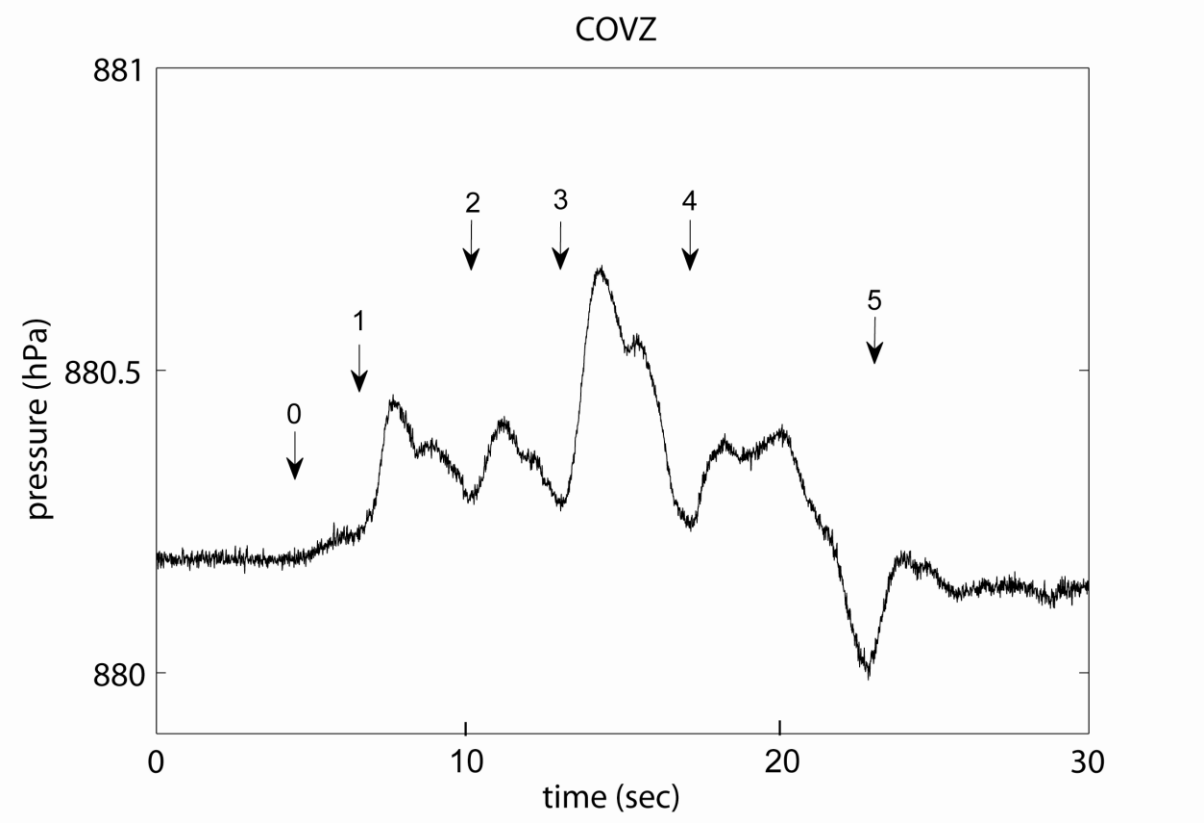

Figure 12. Acoustic data highlighting the start of six coherent phases. Arrows point to the pressure pulse onset for an initial emergent phase (0) followed by 5 impulsive pressure pulses (1 – 5) which are presumed to indicate the onset of eruptions (modified from Jolly et al. 2014).

Table 3. Eruption parameters for each of the five pulses.

	Eruption pulse									
	1		2		3		4		5	
Parameter	**Mean**	**1SD**	**Mean**	**1SD**	**Mean**	**1SD**	**Mean**	**1SD**	**Mean**	**1SD**
Particle density (kg/m³)	2170	386	2170	386	2170	386	2170	386	2170	386
Particle diameter (m)	0.36	0.23	0.36	0.23	0.36	0.23	0.36	0.23	0.36	0.23
Initial particle velocity (m/s)	200	50	200	50	200	50	200	50	200	50
Inclination angle (degree)		10		10		20		10		10
Rotation angle (degree)	30	0	45	0	70	0	20	0	20	0
Displacement of ejection points from the vent centre (m)	0	20	0	18	0	25.2	0	33.2	0	24.4
[1]Number of particles per burst	2649	0	662	0	6621	0	2649	0	662	0
Direction (North is 0 deg)	110	0	22.5	0	285	0	0	0	245	0

[1]Based on acoustic energy

The model requires vent area and location as a control on the ejection of particles (termed by Tsunematsu et al. as the displacement of ejection points from the vent centre). Together, the geomorphology of the fissure area, eyewitness accounts, DEM and LiDAR mapping were used to infer possible vent locations. The vent location of Pulse 1 is inferred to be at the eastern end of the eastern fissure, based on the eyewitness accounts. The second pulse originated from the eastern end of the west segment of the fissure, inferred from the arcuate features (potential vents) observed in the area. Lube et al. (2014) and Procter et al. (in press) also note crater-like features within the western fissure. Consistent with a low angled jet (from horizontal), as described by eyewitnesses, Pulse 3 is proposed to have originated from the top of the debris avalanche scarp where it meets the western fissure, where a small depression can be seen in the DEM (Procter et al. in press). To achieve such a low angled jet (from horizontal), as described by eyewitnesses, the vent had to be located outside the fissure to not be hindered by the fissure walls. Subsidence may have accompanied this pulse and helped to form the western end of the fissure. Based on the eyewitness accounts and differential LiDAR, Pulse 4 originated from Upper Te Maari crater (Procter et al. in press). The location of Pulse 5 is discussed later.

3.4.4.1.2 NUMBER OF ERUPTED PARTICLES

The number of erupted particles, important in controlling the impact crater density, was based on the number of impacts mapped from both the orthophotos and through ground-truthing. Two discrepancies are apparent from the earlier analyses:

1. The ground-truthed distribution underestimates the occurrence and number of very large craters (no craters >6 m in diameter were found), though craters up to 10.8 m in diameter were mapped on the orthophotos (Figure 10C).
2. The orthophoto distribution underestimates the occurrence and number of very small craters (only 19% of craters are <1.5 m in diameter, compared to the 74% found ground-truthing; Figure 10C).

To correct these discrepancies and approximate the true number of particles ejected, the frequency and size distribution data is combined from each of the mapping techniques (Figure 10C). Confidence is placed in the relative abundance of craters >2.5 m mapped on the orthophotos (which is estimated as a conservative lower bound for which craters can be identified correctly on the orthophotos) and also in the relative abundance of all ground-truthed craters <2.5 m in diameter. Therefore the relative ratios of the number of ground-truthed craters <2.5 m in each size bracket (e.g. 0 – 0.5 m) to the number of ground-truthed craters in the 2.5 – 3 m size bracket can be calculated. These ratios can then be used to recalculate the number of mapped orthophoto craters in the 0 – 2.5 m diameter range by multiplying each ratio by the number of craters mapped using the orthophotos in the 2.5 – 3 m size bracket (Figure 10C). This results in a total of 13,243 ballistics ejected in the August eruption.

The number of particles ejected in each pulse is defined in this model by the acoustic energy (Figure 12). The acoustic amplitude is assumed to reflect eruption energy, with the relative energy reflecting the relative number of particles ejected. For example, the third pulse was the largest and expended ~50% of the eruption energy, and is therefore assumed to have ejected 50% of the total number of ballistics (defined in 'Number of particles per burst' in Table 3 as 6621). Another way to calculate the eruption energy for each pulse is to use the power law relationship (in which the vent area is related to the eruption energy) defined and used by Goto et al. (2001) and Lube et al. (2014). However, as there is not a high degree of certainty surrounding the proposed vent areas, this method was not applied and instead the acoustic energy method was used.

3.4.4.1.3 PARTICLE DENSITY AND DIAMETER

Particle density and diameter are important controls on the transport of the erupted particles. In the field, four main block lithologies (dense andesite lava, vesicular scoria or lava, polylithic breccia, and angular intermediate density andesite lava) were observed and sampled. Density measurements were taken of each type and assigned to the appropriate blocks mapped in the field (c.f. Breard et al. 2014). A mean density (weighted by occurrence) calculated from all mapped blocks (2,170 kg/m^3), and the standard deviation (386 kg/m^3), were used for the model particle density (Table 3). The mean (0.36 m) and standard deviation (0.23 m) particle diameters of all whole blocks found in the field were used (Table 3). These particle diameters are consistent with the mean block diameter (0.38 m) found using the approximate mean corrected crater diameter (1.2 m) and the relationship from Figure 11.

3.4.4.1.4 ROTATION ANGLE

Rotation angles (angle of particle ejection from vertical) for the five pulses were estimated from the eyewitness accounts and mapped crater distribution. Proposed angles were tested until the model runs matched the mapped distribution. The mapped crater distribution shows a slightly higher density of craters towards the north, indicating that the near vertical Pulse 4 was likely ejected at a slight northward angle (~20°). Pulses 1 and 3 correspond to the directed blasts identified by the eyewitnesses. The area of higher crater density found to the WNW (Pulse 3), has a best fit rotation angle of 70°.The area of increased crater density in the ESE (Pulse 1) has a best fit rotation angle of 30° toward the ESE. The inferred Pulse 2, not witnessed by the local residents, likely had a rotation angle close to that of Pulse 1 for it to have been obscured by the preceding pulse. An angle of 45° is therefore suggested as this then reproduces the slightly protruding NNE edge of the ballistic field.

3.4.4.1.5 INCLINATION ANGLE

The inclination angle (defined in the Tsunematsu model as the standard deviation of the rotation angle) is significant in controlling the lateral spread of the impacts. It was initially estimated, based on the concept that a wider distribution of ballistics from an eruption

pulse implied a larger inclination angle. The value was then iteratively refined by fitting the model to the mapped crater distribution. Best fit was achieved by assigning all pulses an inclination angle of 10°, with the exception of Pulse 3 which had a wider area of distribution and was assigned a 20° inclination angle (Table 3).

3.4.4.1.6 PARTICLE COLLISIONS

Inter-particle collision can cause a change in particle trajectories, and in particular, travel distances (Tsunematsu et al. 2013). The transfer of momentum when a larger particle collides with a smaller particle can cause the smaller particle to travel further than its original trajectory. Tsunematsu et al. (2013) found that particles travelled further when only 1 – 2 collisions occurred (more than this caused the opposite effect) and when there was a significant difference in mass between the colliding particles, the smaller particles travelled further and faster. Particle size was found to have increased with distance in the 1977 eruption of the Ukinrek Maars, Alaska, and the August 1997 eruptions at Soufriere Hills, Montserrat (Self et al. 1980; Druitt et al. 2002). Field observations from the August eruption showed a general increase in crater size with distance, though smaller craters were found at similar distances from the vents as larger craters. Therefore particle collision is proposed as a factor influencing particle distribution. To test the effect of particle collisions, two simulations were run comparing the effects of collision and no collision. As expected, smaller particles travelled further in the collision-included model, resulting in smaller mean crater sizes distally than those modelled without collision. In the case with particle collision, the most distal particles also travelled ~100 m further than those modelled without collision. After demonstrating that particle collisions were an important factor in the modelled impact distributions, all subsequent model runs included collision by default.

3.4.4.1.7 INITIAL PARTICLE VELOCITY (V_i)

The initial particle velocity, together with rotation angle, is significant in controlling the radial extent of particles. To determine the velocity, varying speeds (100 – 400 m/s) were tested (incorporating both a mean and standard deviation) and the outputs compared with the mapped distribution. The results from two model runs with initial particle velocities of 200 m/s (Figure 13A) and 400 m/s (Figure 13B) are presented, highlighting substantially

different results. The 200 m/s run produced a more confined spatial distribution than that seen in the field, where only the outlying particles reached the TAC. Particle velocity was then increased to 400 m/s, which produced a spatial distribution that generally matched the mapped distribution, except for the halo of minimal impacts around the vents. However, these initial models assumed particle ejection into a still atmosphere in which displacement of surrounding air or coupling with the gas rich jet phase was not incorporated (Fagents and Wilson 1993; Bower and Woods 1996).

3.4.4.1.8 GAS FLOW VELOCITY (V_g) AND DISTANCE OVER WHICH THIS AFFECTS PARTICLE TRANSPORT

Gas flow velocity and the point where ballistic particles decouple from the eruption column, are important controls on the lateral and radial distribution of the impacts. It is assumed that on eruption the ballistics and gas jet are ejected at the same velocity (i.e. completely coupled) but that the jet velocity then decreases while the ballistics continue to travel faster than the expanding jet due to inertia (the jet and ballistics are partially coupled). Therefore, the relative drag acting on the ballistic particles increases with time. At some point, the particles exit the gas flow completely and are decoupled from this for the rest of their trajectory.

Because the August eruption happened at night, particle and gas flow velocity could not be determined using visual observations. Instead, it needed to be approximated using eruptive features and deposits. Initial model runs assumed eruption into a still atmosphere. To improve the subsequent runs a gas flow function was added that reduced the drag acting on the particle during transport. Since the true value of the gas flow velocity is unknown, and also decreases with time and distance from the vents, a mean value was estimated from the initial particle velocity and the approximate initial pyroclastic surge velocity. The approximate initial pyroclastic surge velocity and the distance from where it was initiated determines the final gas-flow velocity acting on the ballistic particles, and also the radial distance from the vents at which complete decoupling occurs (after which the particles follow entirely ballistic trajectories). Lube et al. (2014) determined initial surge velocities (final gas flow velocity) of up to 100 m/s with the surges initiating between 100 – 1,000 m

from the vents. An approximate initial average particle velocity of 200 m/s and an average gas flow velocity of 150 m/s over a 400 m radius (the effective gas flow radius applied in this model) from eruption to surge initiation (at which point it is assumed the ballistics are completely decoupled from the gas flow) best fit the mapped crater distribution (Figure 13C).

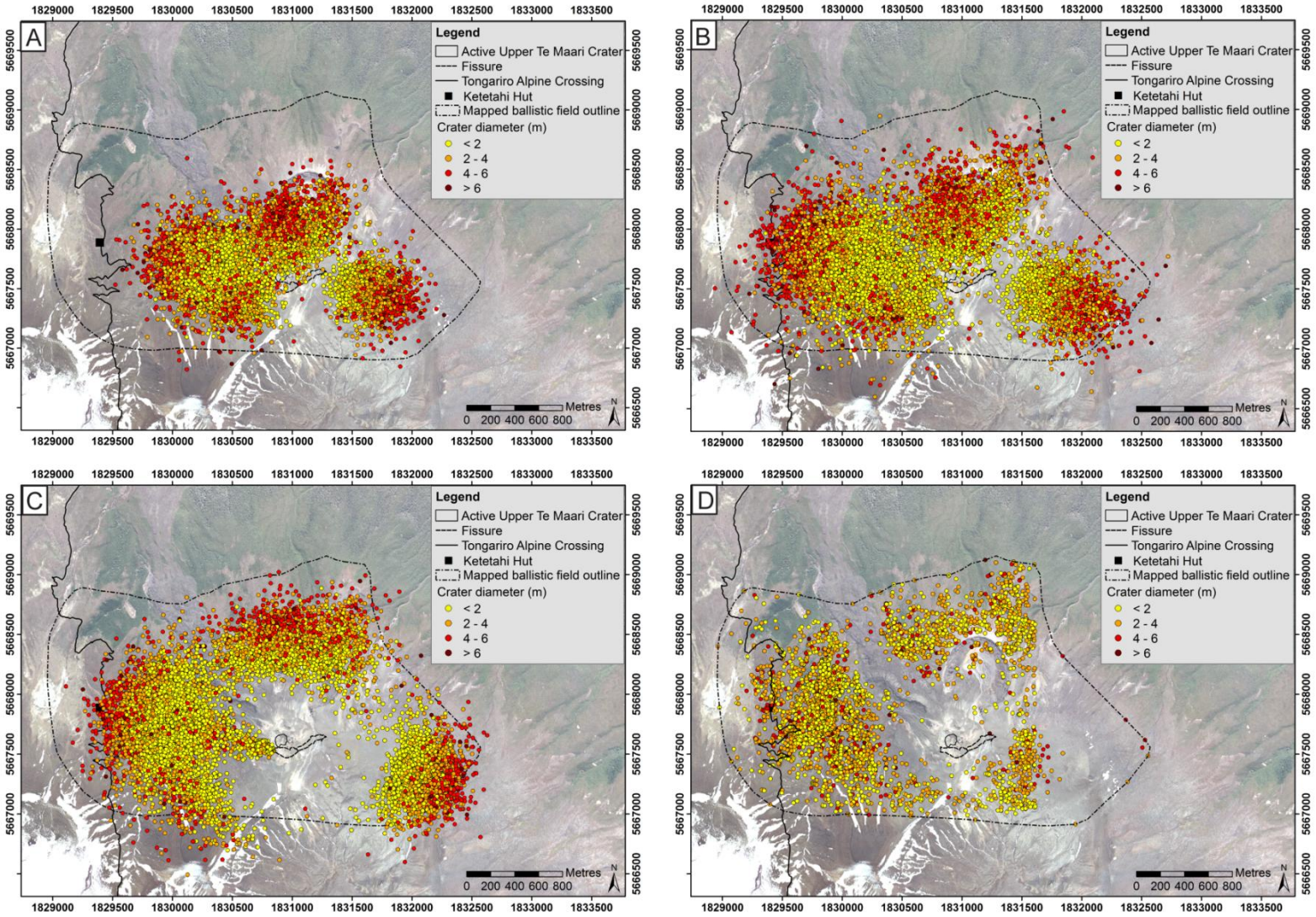

Figure 13. Spatial and size distribution of impact craters from: **A:** modelled eruption using a 200 m/s mean initial particle velocity. **B:** modelled eruption using a 400 m/s mean initial particle velocity. **C:** Best fit modelled eruption with 200 m/s mean initial particle velocity coupled with 150 m/s average gas flow velocity. **D:** Mapped orthophoto distribution (significantly underestimating the true dispersal) from 6 August, 2012 eruption of Upper Te Maari (Figure. 9A). Detailed data from models is available in Appendix B (c – e).

Though the run with an initial particle velocity of 400 m/s fitted the mapped distribution relatively well, it did not include the effects of ballistic and jet coupling (as proposed by Bower and Woods 1996), thus the combination of a 200 m/s initial particle velocity, 150 m/s average gas flow velocity over a 400 m distance and the other aforementioned parameters (Table 3) produced the best fit (based on visual comparison) with the mapped distribution. In order to reduce the number of variables in the model runs, the same velocity (both initial particle and gas flow) and standard deviation is assumed for all pulses. The best fit is presented within this constraint.

Particles in the best-fit model reach the same distances as the orthophoto mapped distribution and a radial area of minimal deposition (of predominantly larger impacts) surrounding the vents was produced – a feature also noted in the analysis of the mapped distribution. This feature is attributed to the coupling of the gas flow and ballistic particles which reduces the drag acting on particles and carries the particles further before deposition. De'Michieli Vitturi et al. (2010) also noted an increase in travel distance with the inclusion of a background flow field in their modelling. The modelled Pulse 1 represents the poorest fit to particle travel distance. For this pulse the minimum modelled particle travel distance is greater than the mapped distribution in the area. This may indicate that it had a slower velocity than the other pulses, and in the case of Pulse 1 the assumption of similar velocities of the different pulses may not be ideal. However, this would require many more model runs and Monte Carlo modelling to confirm.

The best-fit parameters outline the most appropriate scenario based on the available independent data, observations and the 49 inverse models run investigating initial particle velocity, gas flow velocity, angle of particle ejection, and eruption directionality. Future ballistic modelling (using this model) would benefit from more quantitative analyses and Monte Carlo analyses to confirm these findings. The best fit parameters for the 6 August, 2012 Upper Te Maari eruption are presented in Table 3.

In summary the results of the study show:

1. The impact crater size and count is significantly underestimated considering only orthophoto data.

2. Impact crater density and the shape of the ballistic field support multiple eruption pulses and directions consistent with observations.
3. Parameterised Tsunematsu modelling including the effect of drag on particles and entrainment with the gas flow reproduces the spatial distribution including ballistic field asymmetry and a proximal halo of low impact density.

3.5 DISCUSSION

3.5.1 MAPPED BALLISTIC IMPACT DISTRIBUTION

The variation in mean crater size at varying azimuths from the vents possibly reflects different sources and sizes of eruption. Breard et al. (2014) describe the fissure walls as being composed of beds of poorly sorted breccias, diamictons and agglutinates that vary in the size of the clasts (up to 1 m in diameter blocks at the saddle between the western and eastern segments of the fissure), thickness, lateral extent and degree of hydrothermal alteration. The inner wall stratigraphy of Upper Te Maari Crater is described by Hobden (1997) as composed of an upper bedded tuff breccia underlain by a massive mega-block tuff breccia with lithics <2 – 3 m in diameter. It is possible that the variation in the mean crater sizes reflects the local deposit properties at each of the eruption source localities: Upper Te Maari Crater is likely the source of Pulse 4 which produced the northern ballistic field; and Pulses 3 and 5 likely originated from the western segment of the fissure, producing the western ballistic field. A large directed blast is thought to have produced the W-NW ballistic distribution, with a smaller eruption pulse from Upper Te Maari crater the source of the northern section of the field. The blocks that produced the W-NW impact field also likely experienced more fragmentation from the larger, more explosive eruption, than those in the north of the field. This is consistent with experimental results that show larger eruption energies produce smaller grain-sizes (Kueppers et al. 2006).

3.5.2 EFFICIENCY OF EXPLOSION ENERGY CONVERSION INTO BALLISTIC KINETIC ENERGY

The presented field and modelling results can be taken further to help constrain energy conversions during hydrothermal eruptions. The crater diameter frequency distribution (Figure 10C) and the empirical relationship of crater diameter vs block size (Figure 11) can

be combined with the total number of ballistics to compute a block size frequency curve and the total numbers of blocks for each size interval. Using the mean particle density, the total ballistic mass can be constrained to ~1.2×10^6 kg. The total kinetic energy expended by the ballistics can then be calculated using the initial particle velocity of 200 m/s, resulting in a total of 1.7×10^{10} Nm. This is roughly 0.1% of the bulk explosion energy released during the eruption (c.f. Jolly et al. 2014; Lube et al. 2014). In comparison, the efficiency of energy conversion into the kinetic energy of the blast-like surges is almost an order of magnitude higher.

3.5.3 BALLISTIC TRAJECTORY MODEL

Model parameters for four pulses of eruption have been presented; however, the proposed best-fit model includes the impact distributions from five eruption pulses. The 5th pressure pulse distinguished by Jolly et al. (2014) is preceded by a negative release of energy before releasing ~5% of the total eruption energy (Figure 12). They suggest the negative release may be the result of subsidence in the vent region or the entrainment of air into the eruption column from the 4th pulse. The 5th pulse was not observed by the eyewitnesses, like the 2nd pulse, and no evidence of an associated surge has been found (though a surge may not have been produced in this instance). Nevertheless, in this analysis the mapped distribution could be best reproduced by including all five of the eruption pulses and assuming each produced ballistics. Without the ejection of ballistics in Pulse 5, the south-western extent of the ballistic field could not be reproduced. An increased crater density in the WSW – SW indicates a slightly angled blast (Figure 9) and subsequently an ejection angle of ~20° produced the best fit in the Tsunematsu model. The final (5th) event in the sequence is thought to have originated from the middle of the western segment of the fissure, where a vent-like feature is observed missing material.

Given the good correspondence between the modelled parameters and the observed ballistic data, the new model can be utilised for assessing the ballistic hazard from future eruptions. In the next section, the calibrated model is applied to two eruption scenarios for the Upper Te Maari vent region, and the potential vulnerability from such eruptions to hikers on the TAC is examined.

3.5.4 APPLICATION OF THE CALIBRATED MODEL TO FUTURE BALLISTIC HAZARD FROM UPPER TE MAARI

Analysis of future ballistic hazard and vulnerability along the TAC is possible through the application of the calibrated Tsunematsu model. Risk assessments completed following the 2012 eruptions considered three possible future eruption scenarios: (1) a smaller eruption, based on the November 2012 event, (2) an eruption of the same size as the August eruption, and (3) a magnitude larger eruption (Jolly and Taig 2013; Jolly et al. in press). This approach is followed in this study, analysing the particle distribution from each of the scenarios modelled. Magnitude, in this case, defines the quantity of ballistics produced e.g. a magnitude larger scenario produces 10 times the number of ballistics than the August eruption (reflecting an increase in eruption energy). Accompanying this is an increase or decrease in both initial particle and gas velocities, as well as flow radius. Applying a frequency-magnitude split of the earlier determined, more simplistic, average frequency of eruption (0.15 per year) to estimate the probability of occurrence in the next year of the three possible future scenarios, produces probabilities of 0.139, 0.01 and 0.001 respectively.

A smaller eruption, based on the 21 November, 2012 eruption of Upper Te Maari, was modelled to analyse the hazard associated with smaller eruptions (Figure 14A). In this scenario, only one eruption pulse was generated, from Upper Te Maari Crater. Ten times fewer particles than the August eruption were modelled, at speeds of 100 m/s based on particle velocities from the 1988 - 89 Tokachidake, Japan eruption (with an eruption mass an order of magnitude less than the August eruption; Yamagishi & Feebrey 1994; Woods 1995; Breard et al. 2014 and Procter et al. in press). Particles were ejected vertically, with a 10° inclination angle, similar to the eruption column seen in the November eruption. Video analysis of the 21 November eruption showed finger jets extending up to ~300 m above the vent before being enveloped in the ash column likely representing the point of block decoupling and reflecting a 300 m gas flow velocity radius for the scenario modelled. A 75 m/s average gas flow velocity was applied in this model, averaged from surge velocities of 40 – 90 m/s from similar sized eruptions of Soufriere Hills (Calder et al. 1999) and the aforementioned 100 m/s initial particle velocities.

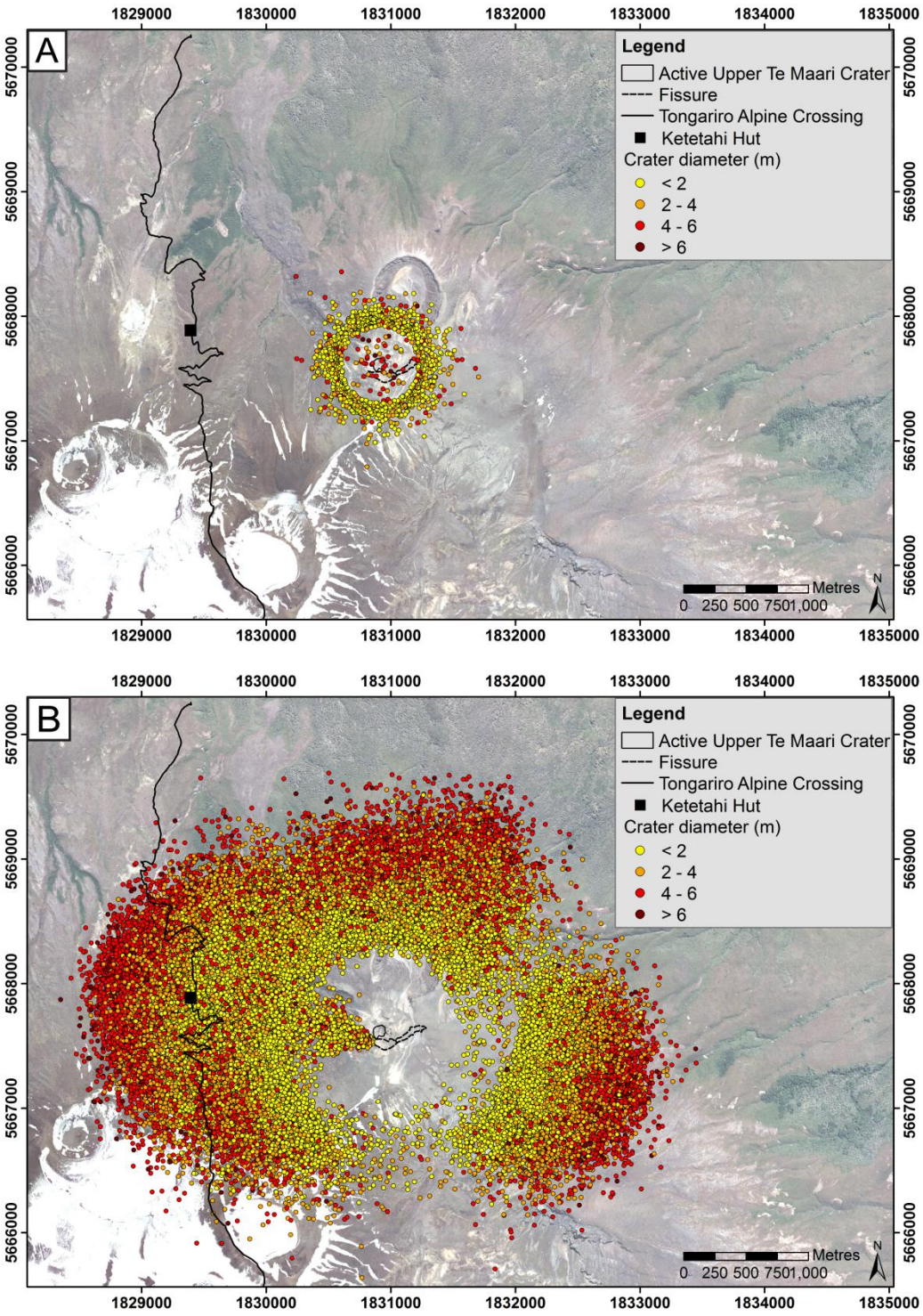

Figure 14. Impact crater distributions from possible future eruption scenarios modelled using the Tsunematsu et al. (2013) ballistic trajectory model (see Appendix B (f – g) for detailed data). **A:** Impact crater size distribution of a smaller eruption similar in size to the November 2012 eruption, with a 100 m/s average initial particle velocity coupled with a 75 m/s average gas flow velocity over a 300 m distance. **B:** Impact crater size distribution of a magnitude larger eruption from Upper Te Maari, with an average initial particle velocity of 400 m/s coupled with an average gas flow velocity of 250 m/s over a 600 m distance.

In the magnitude larger scenario (Figure 14B) all but three of the eruption parameters remained the same as those modelled in the August eruption, as a multiple pulse eruption with directed blasts towards the TAC is also likely in the future. The number of particles ejected in this scenario was increased tenfold (from the August impact estimate) to match the increased eruption magnitude. Initial particle and average gas flow velocities were also increased, to 400 m/s and 250 m/s respectively. Fagents and Wilson (1993) report particle velocities of up to 400 m/s from the magnitude larger 1968 eruption of Arenal volcano (an estimated 2±1 x 10^6 m³ of material was erupted, compared with the 6.3 x 10^5 m³ excavated from the fissure and Upper Te Maari Crater) and accordingly was the value applied in the model. Gas flow velocity in this scenario was derived from a surge velocity of 100 m/s and an initial particle velocity of 400 m/s. Surge velocities of the 1997 Soufriere Hills eruptions (analogous in size to the proposed scenario) ranged up to 90 m/s (Calder et al. 1999). Although the August Upper Te Maari eruption was smaller in size than those of Soufriere Hills, surge velocities are thought to have been up to 100 m/s, thus the faster 100 m/s surge velocity was adopted (Lube et al. 2014). As the distance at which the gas flow no longer influences ballistic trajectory is difficult to estimate and observations of distances of decoupling are rare, a value (600 m) was applied, in line with those found from modelling of clasts coupled with a carrier flow field in de' Michieli Vitturi et al. (2010).

Like the 21 November eruption, the smaller model scenario poses no ballistic hazard to the TAC, with ballistics falling well short of the track. However, the particle distribution from the larger eruption scenario is much denser and more widespread than the August 2012 eruption (Figure 14B) due to the increased particle number. A greater proportion of the track is inundated with ballistics, increasing the area of ballistic hazard and risk. Both of the eruption scenarios display the halo of minimal deposition proximal to the vents, though a wedge radiating toward the west in the larger scenario shows greater deposition due to the low ejection angle of Pulse 3 (70° from vertical). Only larger craters are visible within the halo of the smaller scenario, suggesting that the larger ballistics followed paths uninhibited by coupling with gas flow, with smaller particles carried further before deposition due to gas flow entrainment – a feature not observed in the faster velocity models. Further investigation is needed to understand the relationship between particle size, the distance travelled and the velocity of the gas flow.

3.5.5 BALLISTIC VULNERABILITY ALONG THE TONGARIRO ALPINE CROSSING

The impact distributions from the 6 August eruption and the scenarios modelled here highlight the significant ballistic hazard to the TAC. Around 80,000 people walk the track each year, therefore a key risk management task following the August eruption was to calculate the probability of a person being in an area where a ballistic would cause serious injury or death along the impacted length of the TAC (henceforth the probability of casualty), from possible future eruptions. In their risk assessment, Jolly and Taig (2012) calculated the probability of fatality for the area of track next to Ketetahi Hut. A 7 m^2 radial area of impact hazard was calculated from a block 1 m in diameter, considering only the hazard from crater formation. This calculation was revised in this study, using the average crater diameter found in the field; including the hazard of block fragmentation and production of shrapnel assuming a person is standing at the edge of the crater; and incorporating the hazard along the ballistic flight path prior to impact as impact angles measured were as low as 30° from horizontal.

For the analysis in this study, the area of ballistic hazard (within which 100% casualty is assumed) was calculated using the average crater size (1.2 m found from ground-truthing) and average impact angle (59° from horizontal) produced by the August eruption, to find a mean ballistic hazard area of 8 m^2 per impact (Figure 7B). This value was then divided by the varying impact densities along the TAC to generate conditional probabilities of casualty from each specific eruption scenario (assuming an eruption during the time of exposure). Using the orthophoto mapped August eruption densities as an example, the first major bend in the TAC south of Ketetahi Hut is found to be located in an area with an impact density of 3,000 – 4,000 per km^2 (Figure 9B). This is converted into m^2 resulting in 1 impact per 333 m^2 and 1 impact per 250 m^2 respectively. The probability of casualty can then be calculated, producing a probability along the TAC beside Ketetahi Hut of 0.02 – 0.03 or up to 3% (8/333 = 0.02; 8/250 = 0.03).

The probability of casualty from ballistic strike along the TAC is presented from the mapped distributions, modelled distributions, and the two eruption scenarios (Figure 15). The highest probabilities of being struck are located on the first bend south of Ketetahi Hut in all but the magnitude larger scenario. At this location, the probability of casualty is 2 to 3%

(calculated above) from the orthophoto distribution (Figure 15A). When scaled up to match the ground-truthed impact densities (rounded to a scaling factor of 4 from Table 2), probabilities increase up to 16% (Figure 15B). The best fit model distribution exhibits probabilities of casualty similar to that of the scaled mapped distribution, reflecting the models ability to reproduce the observed impact distributions (Figure 15C). The difference between the orthophoto probabilities and the scaled and modelled probabilities is owed directly to the underestimation of the ballistic density using an 'orthophoto only' approach. Hence a clear outcome of this work is to emphasise the importance of both high resolution orthophotos and ground-truthed data within a sophisticated ballistic modelling paradigm.

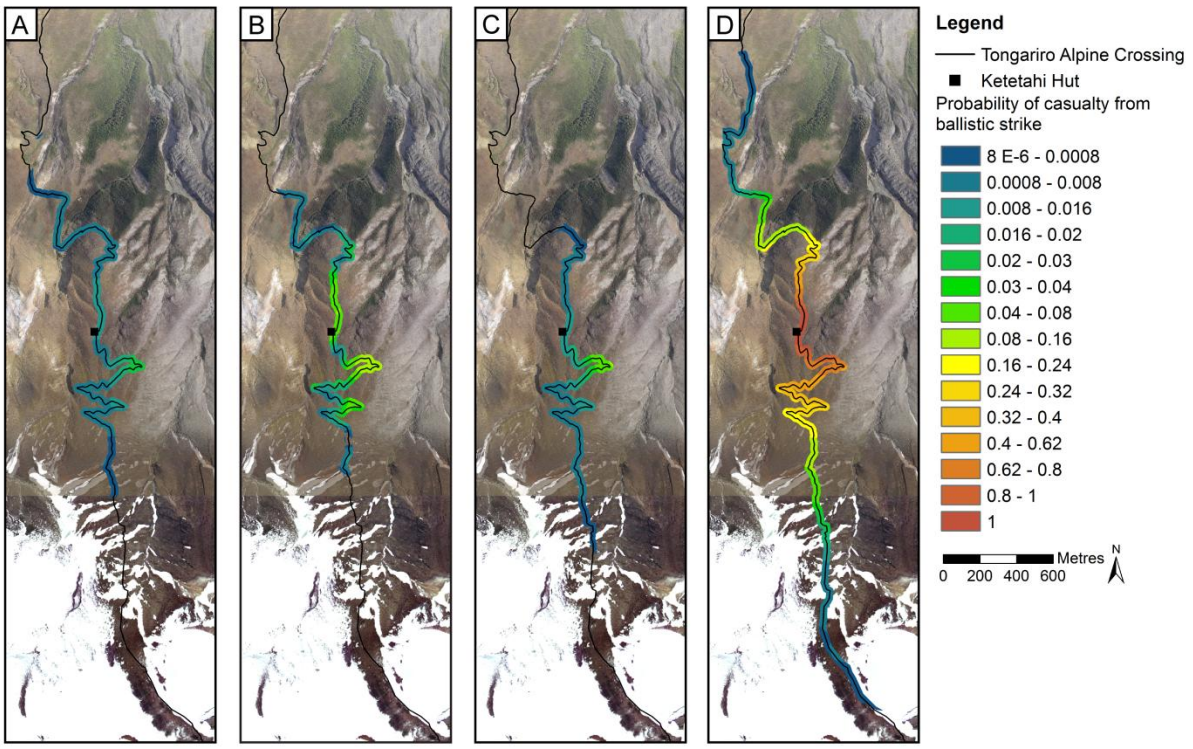

Figure 15. Ballistic vulnerability or probability of casualty assuming an eruption during the time of exposure, along the Tongariro Alpine Crossing calculated using the impact densities from: **A:** Orthophoto mapping; **B:** Orthophoto impact densities scaled to those observed in the field comparisons; **C:** Best-fit model of August eruption; **D:** Magnitude larger eruption scenario.

In the smaller eruption scenario, casualty by ballistic strike on the TAC would not occur, as ballistics did not travel further than ~700 m from the vent. In contrast, the impact densities along the affected TAC in the larger eruption scenario are so high that the probability of casualty reaches 100% (along a 150 m length north and 75 m length south of Ketetahi Hut).

Additionally, the length of the TAC located within the ballistic impact field in this scenario increased by 50% from 2.6 km found in the August eruption, to 5.2 km (Figure 15D). It must be emphasized that the scenarios modelled are only two possibilities out of countless potential eruption scenarios, and that slight changes in the eruption parameters modelled (such as number of ejected particles or direction of the blast) can drastically change the impact density and, consequently, the probability of casualty. The ballistic trajectory model therefore is an important tool in assessing future ballistic hazard and risk from Upper Te Maari.

3.6 SUMMARY

The 6 August 2012 hydrothermal eruption of Upper Te Maari Crater, Tongariro ejected blocks over a 6 km² area in which ~2.6 km of the Tongariro Alpine Crossing is located. The distribution of ballistic impact craters was mapped through a combination of orthophoto analysis and field surveys. With the application of a new ballistic trajectory model to the mapped distributions, monitoring data and eyewitness accounts, eruption parameters were constrained and the August ballistic distribution successfully reproduced. The model, now calibrated with the 6 August eruption, was used to assess future ballistic hazard from Upper Te Maari and the probability of casualty during these eruptions. Conclusions from this chapter are presented in Chapter 5.

CHAPTER 4: LIMITATIONS AND FUTURE WORK

Chapter 4 discusses the limitations of the research presented in Chapter 3. It also discusses opportunities for future research directions.

Volcanic risk assessments require often detailed hazard and vulnerability information to produce a credible result. Simple assessments require minimal inputs, but have high uncertainties. As society demands greater responsiveness, functionality and transparency for volcanic risk assessments, and volcanologists improve their understanding of hazardous processes, there is the opportunity to improve the accuracy of the risk assessments. However, this requires risk models to become increasingly sophisticated. They rely on models (numeric, empirical or statistical) to forecast the extent and intensity of hazards; and on detailed vulnerability information, including temporal and spatial location of assets and asset's performance when exposed to different hazard intensities (i.e. fragilities). However, as with all scientific studies there are limitations to what data can be collected or is available, of our understanding of how processes influence system results and the performance of models replicating a real system or process.

The following paragraphs outline and discuss limitations of the research undertaken in this study and identify how future research opportunities can address some of these limitations.

4.1 BALLISTIC MODELLING.

As with any numeric model, limitations are based on the accuracy of the input parameters and the assumptions made in the mathematics of the model, many of which were discussed in Chapter 3. However, the well constrained best fit ballistic distribution in comparison with the mapped distribution gives confidence in the models assumptions and inputs (Section 3.4.4.1.8).

The ballistic model required a number of input parameters to produce a ballistic distribution that could be compared to the mapped distribution, constraining eruption parameters and calibrating the model (Section 3.4.4.1). Inverse modelling produced a best-fit scenario of all eruption parameters that matched the mapped distribution. One assumption of the 6

August best-fit scenario which could be improved on by further modelling is that all eruption pulses were erupted at similar mean velocities. The best fit distribution (Figure 13C) illustrates that this assumption was valid for Pulses 2 - 5 as these distributions relatively fit the mapped distribution, however, Pulse 1 does not. The modelled Pulse 1 distribution has a greater minimum travel distance than the mapped distribution, either due to the modelled average initial particle velocity being too high or the rotation angle being too shallow. Eyewitnesses stated Pulse 1 was ejected at an angle <45° from vertical, so accordingly steeper angles between 30° (the best fit angle) and 20° were tested (angles <20° were considered too close to vertical) though these did not improve the fit of the distribution. Therefore, particle velocity was the parameter attributed to the inconsistent distribution. In future when calibrating mapped distributions with modelled scenarios, velocity should be tested separately for each pulse, rather than assuming all pulses were erupted at the same velocity. However, time constraints invoked by computing time limited the number of models that could be run in this study.

Another limitation of the best fit scenario is that a semi-quantitative deterministic approach was taken to determine eruption parameters. Though variations of each parameter were tested (49 models in total), it was not done systematically, quantitatively or statistically, rather best fit was determined from visual comparison. To support and confirm these findings probabilistic analyses, such as Monte Carlo analyses, need to be completed. This was not possible in the available timeframe, though is the goal of future work.

Many models prior to 1990s overestimated particle velocity assuming ballistics were ejected into a still atmosphere. As ballistics are initially partially coupled with the expanding jet, drag on particles is reduced until decoupling from the jet (Section 2.6). To introduce a zone of reduced drag around the vent, as included in previous models, two functions were added to the model: an average gas flow velocity and the radius over which the gas flow acts to reduce the drag (partial coupling of the gas flow with the ballistics) (Section 3.4.4.1.8). These functions, however, carry a limitation. They assume that the expanding gas flow travels at a constant velocity, though slower than the particle velocity, throughout a designated distance of reduced drag. This is not realistic as it is widely accepted that the gas flow and entrained ballistics are coupled initially, travelling at the same velocity, progressively

decelerating and decoupling. Ballistics retain much of their momentum while the gas jet decompresses and decelerates at a faster rate (Fagents and Wilson 1993; Bower and Woods 1996; Mastin 2001). Future use of the model would benefit from the introduction of a gas flow velocity decay rate or, alternately, a drag increase rate rather than set distances and speeds at which the gas interacts with the particle. This is ongoing work with Kae Tsunematsu, the creator of the model, which will introduce this code into the model.

4.2 HAZARD PROCESS

In situations where only impact craters can be easily mapped as blocks may have shattered on impact or cannot be found (as was the case for this study), approximations of ballistic size may be made from crater size using a relationship between the two (Section 3.4.3). Investigations into whether a relationship could be found between block size and crater size found a weak power-law relationship from a broad spread of data. It became apparent that there may have been two trends in the data, one between 0 and 2 m crater diameter, and the other >2 m, though only one relationship could be applied to the data (the overall relationship). Block lithology/density was thought to be controlling the different trends, however this could not be confirmed (Type 2 blocks only created craters <2 m from the locations sampled, though Type 1 produced craters between 0 and 6 m in diameter). Future work on this relationship should investigate the effect substrate type and strength as well as vegetation type and thickness has on crater size and whether this could explain the two relationships found. An experimental set up including a pneumatic “volcano canon” has been developed at the University of Canterbury to investigate these parameters. More data points on the lithology and crater size would also be beneficial to further constrain this relationship.

4.3 VULNERABILITY

Calculations of vulnerability of hikers along the TAC included the area of hazard from an individual ballistic (section 3.3.4). A component of this area of hazard is a debris/shrapnel apron (Figure 7). It is proposed that serious injury or death could occur in this radius from pieces of shattered ballistic (secondary ballistics) or ejecta from the crater though the extent of potential injuries or threshold at which this would occur is not known. Further research

and experimentation is needed to quantify the speed and energy of the shrapnel as well as at what speeds and pressures cause injury or death. The new experimental apparatus at the University of Canterbury has also been designed to assess this.

CHAPTER 5: CONCLUSIONS

Chapter 5 presents conclusions of this thesis. It primarily draws from the research presented in Chapter 3, but also the wider context of volcano risk management as presented in Chapters 1 and 2.

In this study ballistic hazard from Upper Te Maari Crater, Tongariro is assessed through:

1) A review of ballistic distributions mapped around volcanoes.
2) A review of the eruptive history of Upper Te Maari and its eruptive styles and frequencies.
3) Field and orthophoto mapping of the 6 August, 2012 ballistic impact crater distribution.
4) Calibration of the Tsunematsu ballistic trajectory model using the 6 August ballistic impact distribution, and refinement of eruption parameters through inverse modelling.
5) Forward modelling of three possible future eruption scenarios using the calibrated Tsunematsu model.
6) Vulnerability analyses along the Tongariro Alpine Crossing, incorporating variations in ballistic impact density along the impacted track.

The size, shape and density of the ballistic impact field are critical pieces of data for a ballistic hazard assessment. The review of ballistic distributions from volcanoes around the world showed that in most cases the distribution of ballistics from individual eruptions are strongly asymmetric around the vent from directed eruptions and the density of impacts is rarely reported.

The Te Maari vents have been the source of large Plinian eruptions in the past, though newspaper articles and early notes from local observers and scientists have shown that the recent history of Upper Te Maari has been dominated by small hydrothermal or phreatomagmatic events. An average frequency of eruption of 0.15 per year was calculated using all 22 historical eruptions over 145 years.

Orthophoto analysis and field mapping revealed that a 6 km^2 asymmetric ballistic impact field was produced in the 6 August, 2012 eruption of Upper Te Maari. Multiple pulses of

eruption varying in directionality were witnessed by nearby residents, noted in the acoustic record and supported by the ballistic field's asymmetry and areas of increased impact crater density in the W - NW, N - NNE and ESE. Initial analysis of orthophotos taken after the eruption located 3,587 impact craters, though ground truthing of selected sites revealed this an underestimation with the number of ejected ballistics found to be on average approximately four times greater (~13,200). This was in large part due to resolution limits of the orthophotos in which craters <2 m in diameter proved difficult to identify.

Eruption parameters were constrained and the August ballistic distribution successfully reproduced with the application of a new ballistic trajectory model to the mapped distribution, combined with monitoring data and eyewitness accounts. An average initial particle velocity of 200 m/s partially coupled with the expanding jet over a 400 m distance, travelling at, on average, 150 m/s was found to produce a ballistic distribution that best fit the mapped distribution. The inclusion of a gas flow velocity function produced a zone of reduced drag around the vent and recreated the vent proximal radial zone of minimal impacts seen in the mapped distribution. This suggests that the initial entrainment of ballistics in the expanding jet is an important parameter in the vent-proximal transport of ballistic particles. Now calibrated, the model was used to assess two additional possible scenarios of future ballistic hazard.

A smaller eruption similar in size to the November 2012 eruption and a magnitude larger eruption (than the 6 August) were modelled to assess ballistic hazard from a range of possible future eruption sizes. Ballistics ejected in the smaller eruption did not reach the TAC, posing no hazard to hikers. The length of TAC inundated with ballistics increased by 50% to 5.2 km in the larger scenario, with tens times more ballistics ejected than the August eruption.

As ~80,000 people hike the track each year, vulnerability analyses were included in the hazard assessment. Probability of casualty (serious injury or death) along the impacted TAC (assuming eruption during time of exposure) ranged up to 0.16 or 16% in the modelled August eruption and reached 100% near Ketetahi Hut in the larger scenario.

The capability of the calibrated model to create and model future ballistic hazard scenarios and produce distribution maps to allow comparison with eruption distributions is therefore

a powerful tool that can be used to improve management of ballistic hazard and risk at Upper Te Maari as well as at other volcanoes worldwide.

REFERENCES

Alatorre-Ibargüengoitia MA, Delgado-Granados H 2006. Experimental determination of drag coefficient for volcanic materials: Calibration and application of a model to Popocatépetl volcano (Mexico) ballistic projectiles. Geophysical Research Letters 33(11): L11302.

Alatorre-Ibargüengoitia MA, Delgado-Granados H, and Farraz Montes IA 2006. Hazard zoning for ballistic impact during volcanic explosions at Volcan de Fuego de Colima (Mexico). GSA Special Papers 402: 209 – 216.

Alatorre-Ibargüengoitia MA, Delgado-Granados H, Dingwell DB 2012. Hazard map for volcanic ballistic impacts at Popocatépetl volcano (Mexico). Bulletin of Volcanology 74(9): 2155–2169.

Baxter P, Gresham A 1997. Deaths and injuries in the eruption of Galeras Volcano, Colombia, 14 January 1993. Journal of Volcanology and Geothermal Research 77: 325–338.

Berryman K, Villamor P 1999. Spatial and temporal patterns of active faulting in the Taupo Volcanic Zone, New Zealand. Geological Society of New Zealand Miscellaneous Publication 107A: 15.

Bibby HM, Caldwell TG, Davey FJ 1995. Geophysical evidence on the structure of the Taupo Volcanic Zone and its hydrothermal circulation. Journal of Volcanology and Geothermal Research 68: 29–58.

Birkmann J 2013. Exposure to natural hazards. In: Bobrowsky, PT (ed.) Encyclopedia of Natural Hazards. Springer Netherlands: 305-306.

Blong R J 1984. Volcanic hazards: A sourcebook on the effects of eruptions. Orlando: Academic Press. 424 p.

Blong R 1996. Volcanic hazards risk assessment. In: Scarpa R, Tilling RI eds. Monitoring and mitigation of volcano hazards. New York, USA, Springer: 675-698.

Bower S, Woods A 1996. On the dispersal of clasts from volcanic craters during small explosive eruptions. Journal of Volcanology and Geothermal Research 73: 19–32.

Breard ECP, Lube G, Cronin SJ, Fitzgerald R, Kennedy B, Scheu B, Montanaro C, White JDL, Tost M, Procter JN, Moebis A 2014. Using the spatial distribution and lithology of ballistic blocks to interpret eruption sequence and dynamics: August 6 2012 Upper

Te Maari eruption, New Zealand. Journal of Volcanology and Geothermal Research. DOI: 10.1016/j.jvolgeores.2014.03.006.

Calder ES, Cole PD, Dade WB, Druitt TH, Hoblitt RP, Huppert HE, Ritchie L, Sparks RSJ, Young SR 1999. Mobility of pyroclastic flows and surges at the Soufriere Hills Volcano, Montserrat. Geophysical Research Letters 26(5): 537 – 540.

Carter L 1980. NZ regional bathymetry 1:6,000,000 (2nd ed.). NZ Oceanographic Institute Chart. Misc. Series 15. Department of Scientific and Industrial Research, Wellington, New Zealand.

Cole JW, Lewis KB 1981. Evolution of the Taupo-Hikurangi subduction system. Tectonophysics 72:1-21.

Christenson BW, Britten K, Mazot A, Fitzgerald J 2013. The 2012 eruption of Te Maari: Pre- and post-eruption gas signatures from the magmatic-hydrothermal system. Taupo District Council Offices, Turangi, New Zealand: Te Maari day - a workshop to discuss scientific advances from the 2012 Te Maari eruptions, 22 Mar 2013. In: GNS Miscellaneous Series 66.

Cole JW, Nairn IA 1975. Catalogue of the active volcanoes and solfatara fields of New Zealand. International Association of Volcanology and Chemistry of the Earth's Interior, Rome, Italy: Catalogue of the active volcanoes of the world including solfatara fields, 22: pp. 156.

Cole JW 1978. Andesites of the Tongariro volcanic centre, North Island, New Zealand. Journal of Volcanology and Geothermal Research 3: 121- 153.

Cole JW, Graham IJ, Hackett WR, Houghton BF, 1986. Volcanology and petrology of the Quaternary composite volcanoes of Tongariro Volcanic Centre, Taupo Volcanic Zone. Bulletin - Royal Society of New Zealand 23: 224 – 250.

Cole JW 1990. Structural control and origin of volcanism in the Taupo volcanic zone, New Zealand. Bulletin of Volcanology, 52: 445–459.

Cowan J 1927. The Tongariro National Park, New Zealand. Tongariro National Park Board, Wellington. 156 p.

Crozier MJ, Glade T 2005. Landslide hazard and risk: issues, concepts and approach. In: Glade, T, Anderson, MG, Crozier, MJ, eds. Landslide hazard and risk. Chichester, England, Wiley. 802 p.

Crouch J, Pardo P, Miller CA 2014. Dual Polarisation C-Band Weather Radar Imagery of the 6 August 2012 Te Maari Eruption, Mount Tongariro, New Zealand. Journal of Volcanology and Geothermal Research. DOI: 10.1016/j.jvolgeores.2014.05.003.

Cutter SL 2013. Vulnerability. In: Bobrowsky, PT ed. Encyclopedia of Natural Hazards. Springer Netherlands: 1088-1090.

Delgado-Granados H, Cardenas Gonzalez L, Piedad Sanchez N 2001. Sulfur dioxide emissions from Popocatepetl volcano (Mexico): case study of a high-emission rate, passively degassing erupting volcano. Journal of Volcanology and Geothermal Research 108: 107–120.

DeMets C, Gordon RG, Argus DF, Stein S 1994. Effect of recent revisions to the geomagnetic reversal time scale on estimates of current plate motions. Geophysical Research Letters 21: 2191–2194.

de' Michieli Vitturi M, Neri A, Esposti Ongaro T, Lo Savio S, Boschi E 2010. Lagrangian modeling of large volcanic particles: Application to Vulcanian explosions. Journal of Geophysical Research 115(B8), B08206.

Dominguez-Cuesta MJ 2013. Susceptibility. In: Bobrowsky PT ed. Encyclopedia of Natural Hazards. Springer Netherlands: 988.

Druitt TH, Kokelaar BP 2002. The eruption of Soufriere Hills Volcano, Montserrat, from 1995 – 1999. Geological Society, London, Memoirs 21: 281 – 306.

Fagents SA, Wilson L 1993. Explosive volcanic eruptions—VII. The ranges of pyroclasts ejected in transient volcanic explosions. Geophysical Journal International 113: 359–370.

Fleming CA 1953. The geology of Wanganui subdivision. New Zealand Geological Survey bulletin, 52: 362 p.

Friedlaender B 1898. Some notes on the volcanoes of the Taupo District. Transactions of the New Zealand Institute 31: 498-310.

Fudali RF, Melson WG 1972. Ejecta velocities, magma chamber pressure and kinetic energy associated with the 1968 eruption of Arenal volcano. Bulletin of Volcanology 35: 383 – 401.

Gamble JA, Wood P, Price RC, Smith IEM, Waight TE 1999. A fifty year perspective of magmatic evolution on Ruapehu volcano, New Zealand: verification of open system behaviour in an arc volcano. Earth and Planetary Science Letters 170: 301–314.

Graham IJ, Cole JW, Briggs RM, Gamble JA, Smith IEM 1995. Petrology and petrogenesis of volcanic rocks from the Taupo Volcanic Zone: a review. Journal of Volcanology and Geothermal Research 68: 59–87.

Graham IJ, Hackett WR 1987. Petrology of calc-alkaline lavas from Ruapehu volcano and related vents, Taupo Volcanic Zone, New Zealand. Journal of Petrology 28: 531-657.

Gregg DR 1960. The geology of Tongariro subdivision. N.Z. Geological Survey Bulletin 40: 152 p.

Goto A, Taniguchi H, Yoshida M, Ohba T, Oshima H 2001. Effects of explosion energy and depth to the formation of blast wave and crater: Field explosion experiment for the understanding of volcanic explosion. Geophysical Research Letters 28(22): 4287–4290.

Gurioli L, Harris AJL, Colo L, Bernard J, Favalli M, Ripepe M, Andronico D 2013. Classification, landing distribution, and associated flight parameters for a bomb field emplaced during a single major explosion at Stromboli, Italy. Geology 41(5): 559–562.

Hill H, 1891. Tongariro, Ngauruhoe and Ruapehu as volcanic cones. Report of the third meeting of the Australasian Association of Advanced Sciences, pp. 162-172.

Hill, H., 1892. Ruapehu and Ngauruhoe. Transactions of the New Zealand Institute 24: 603-625.

Hill H 1893. The volcanic outburst at Te Mari, Tongariro, in November, 1892. Transactions of the New Zealand Institute 26: 388-392.

Hitchcock DW, Cole JW 2007. Potential impacts of a widespread subplinian andesitic eruption from Tongariro volcano, based on a study of the Poutu Lapilli. New Zealand Journal of Geology and Geophysics 50(2): 53–66.

Hobden BJ 1997. Modelling magmatic trends in time and space: eruptive and magmatic history of Tongariro Volcanic Complex, New Zealand. PhD Thesis, University of Canterbury, Christchurch, pp 508.

Hobden BJ, Houghton BF, Lanphere MA, Nairn IA 1996. Growth of the Tongariro volcanic complex: New evidence from K-Ar age determinations. New Zealand Journal of Geology and Geophysics, 39(1): 151–154.

Hobden BJ, Houghton BF, Davidson JP, Weaver SD 1999. Small and short-lived magma batches at composite volcanoes: time windows at Tongariro volcano, New Zealand. Journal of the Geological Society, London 156: 865–868.

Houghton BF, Swanson DA, Carey RJ, Rausch J, Sutton AJ 2011. Pigeonholing pyroclasts: Insights from the 19 March 2008 explosive eruption of Kilauea volcano. Geology 39(3): 263–266.

Jenkins SF, Spence RJS, Fonseca JFBD, Solidum RU, Wilson TM 2014. Volcanic risk assessment: Quantifying physical vulnerability in the built environment. Journal of Volcanology and Geothermal Research 276: 105–120.

Jolly AD, Jousset P, Lyons JJ, Carniel R, Fournier N, Fry B, Miller C 2014. Seismo-acoustic evidence for an avalanche driven phreatic eruption through a beheaded hydrothermal system: An example from the 2012 Tongariro eruption. Journal of Volcanology and Geothermal Research. DOI: 10.1016/j.jvolgeores.2014.04.007.

Jolly GE, Taig T 2012. Risk assessment for Department of Conservation staff working on the Tongariro Alpine Crossing Track near Ketetahi and for visitors walking on the Tongariro Alpine Crossing Track. GNS Science Consultancy Report 2012/310. 24 p.

Jolly GE, Taig T 2013. Update of risk assessment for visitors walking on the Tongariro Alpine Crossing, February 2013. GNS Science Letter Report. 10 p.

Jolly GE, Keys HJR, Procter JN, Deligne NI in press. Overview of the co-ordinated risk-based approach to science and management response and recovery for the 2012 eruptions of Tongariro volcano, New Zealand. Journal of Volcanology and Geothermal Research.

Kaye G 2008. Volcanic hazard risk assessment for the Riskscape program, with test application in Rotorua, New Zealand, and Mammoth Lakes, USA. Unpublished PhD thesis, University of Canterbury, Christchurch, New Zealand.

Kilgour G, Manville V, Della Pasqua F, Graettinger A, Hodgson KA, Jolly GE 2010. The 25 September 2007 eruption of Mount Ruapehu, New Zealand: Directed ballistics, surtseyan jets, and ice-slurry lahars. Journal of Volcanology and Geothermal Research 191: 1–14.

Kilgour G, Blundy J, Cashman K, Mader HM 2013. Small volume andesite magmas and melt–mush interactions at Ruapehu, New Zealand: evidence from melt inclusions. Contributions to Mineralogy and Petrology 166(2): 371–392.

Kueppers U, Perugini D, Dingwell DB 2006. Explosive energy during volcanic eruptions from fractal analysis of pyroclasts. Earth and Planetary Science Letters 248(3-4): 800–807.

Lube G, Breard ECP, Cronin SJ, Procter JN, Brenna M, Moebis A, Pardo N, Stewart RB, Jolly A, Fournier N 2014. Dynamics of surges generated by hydrothermal blasts during the 6 August 2012 Te Maari eruption, Mt. Tongariro, New Zealand. Journal of Volcanology and Geothermal Research. DOI: 10.1016/j.jvolgeores.2014.05.010.

Maeno F, Nakada S, Nagai M, Kozono T 2013. Ballistic ejecta and eruption condition of the vulcanian explosion of Shinmoedake volcano, Kyushu, Japan on 1 February, 2011. Earth, Planets and Space 65(6): 609–621.

Marker BR 2013. Hazard and risk mapping. In: Bobrowsky PT ed. Encyclopedia of Natural Hazards. Springer Netherlands: 426-435.

Mastin LG 2001. A simple calculator of ballistic trajectories for blocks ejected during volcanic eruptions. US Department of the Interior. US Geological Survey Open File Rep: 01-45.

Minakami T 1942. 5. On the distribution of volcanic ejecta (Part I.): The distributions of volcanic bombs ejected by the recent explosions of Asama. Bulletin of Earthquake Research Institute 20: 65 – 92.

Moebis A, Cronin SJ, Neall VE, Smith IE 2011. Unravelling a complex volcanic history from fine-grained, intricate Holocene ash sequences at the Tongariro Volcanic Centre, New Zealand. Quaternary International 246(1-2): 352–363.

Moebis A 2010. Understanding the Holocene explosive eruption record of the Tongariro Volcanic Centre, New Zealand. Unpublished PhD Thesis, Massey University, Palmerston North.

Nadim F 2013. Hazard. In: Bobrowsky PT ed. Encyclopedia of Natural Hazards. Springer Netherlands: 425-426.

Nairn IA, Kobayashi T, Nakagawa M 1998. The ~10 ka multiple vent pyroclastic eruption sequence at Tongariro Volcanic Centre, Taupo Volcanic Zone, New Zealand: Part 1. Eruptive processes during regional extension. Journal of Volcanology and Geothermal Research 86: 19–44.

Nairn IA, Self S 1978. Explosive eruptions and pyroclastic avalanches from Ngauruhoe in February 1975. Journal of Volcanology and Geothermal Research 3: 36–60.

National Library Papers Past. Retrieved 1 September, 2013 from http://paperspast.natlib.govt.nz/cgi-bin/paperspast?a=q&e=———10-1–0-.

ISO 2009. 31000: 2009 Risk management–Principles and Guidelines. International Organization for Standardization, Geneva, Switzerland.

Pardo N, Cronin SJ, Nemeth K, Brenna M, Schipper CI, Breard E, White JDL, Procter J, Stewart B, Agustín-Flores J, Zernack A, Kereszturi G, Lube G, Auer A, Neall V, Wallace C 2014. Perils in distinguishing phreatic from phreatomagmatic ash; insights into the eruption mechanisms of the 6 August 2012 Mt. Tongariro eruption, New Zealand. Journal of Volcanology and Geothermal Research. DOI: 10.1016/j.jvolgeores.2014.05.001.

Pistolesi M, Rosi M, Pioli L, Renzulli A, Bertagnini A, Andronico D 2008. The paroxysmal event and its deposits. The Stromboli Volcano: An Integrated Study of the 2002 - 2003 Eruption. Geophysica 317–330.

Price RC, Gamble JA, Smith IEM, Stewart RB, Eggins S, Wright IC 2005. An integrated model for the temporal evolution of andesites and rhyolites and crustal development in New Zealand's North Island. Journal of Volcanology and Geothermal Research Res 140: 1–24.

Procter JN, Cronin SJ, Zernack AV, Lube G, Stewart RB, Nemeth K, Keys H in press. Debris flow evolution and activation of an explosive hydrothermal system; Te Maari, Tongariro, New Zealand. Journal of Volcanology and Geothermal Research.

Reyners M 2010. Stress and strain from earthquakes at the southern termination of the Taupo Volcanic Zone, New Zealand. Journal of Volcanology and Geothermal Research 190: 82–88.

Robertson R, Cole P, Sparks RSJ, Harford C, Lejeune AM, McGuire WJ, Miller AD, Murphy MD, Norton G, Stevens NF, Young SR 1998. The explosive eruption of Soufriere Hills Volcano, Montserrat, West Indies, 17 September, 1996. Geophysical Research Letters 25(18): 3429–3432.

Rosenberg R 2012. Volcanic alert bulletin TON-2012/07 – Tongariro Volcano. Retrieved May 15, 2014 from http://info.geonet.org.nz/pages/viewpage.action?pageId=2195849.

Scott B, Fournier N 2012a. Volcanic alert bulletin TON-2012/28 – Tongariro Volcano. Retrieved May 15, 2014 from http://info.geonet.org.nz/pages/viewpage.action?pageId=3801181.

Scott B, Fournier N 2012b. Volcanic alert bulletin TON-2012/30 – Tongariro Volcano. Retrieved May 15, 2014 from http://info.geonet.org.nz/pages/viewpage.action?pageId=3801193.

Scott BJ, Potter SH 2014. Aspects of historical eruptive activity and volcanic unrest at Mt. Tongariro, New Zealand: 1846-2013. Journal of Volcanology and Geothermal Research. DOI: 10.1016/j.jvolgeores.2014.04.003.

Self S, Kienle J, Huot J 1980. Ukinrek Maars, Alaska, II. Deposits and formation of the 1977 craters. Journal of Volcanology and Geothermal Research 7: 39–65.

Sparks RSJ, Aspinall WP, Crosweller HS, Hincks TK 2013. Risk and uncertainty assessment of volcanic hazards. In: Rougier J, Sparks S, Hill L eds. Risk and uncertainty assessment for natural hazards. Cambridge University Press. pp 364 – 397.

Spinks KD, Acocella V, Cole JW, Bassett KN 2005. Structural control of volcanism and caldera development in the transtensional Taupo Volcanic Zone, New Zealand. Journal of Volcanology and Geothermal Research 144: 7–22.

Steinberg GS, Lorenz V 1983. External ballistic of volcanic explosions. Bulletin volcanologique 46(4): 333-348.

Suzuki T, Nishida Y, Niida K 2013. Renovated ballistic equation of ejected blocks and its application to the 1982 and 1983 Sakurajima eruptions. Bulletin of the Volcanological Society of Japan 58(1): 281–289.

Taddeucci J, Scarlato P, Capponi A, Del Bello E, Cimarelli C, Palladino DM, Kueppers U 2012. High-speed imaging of Strombolian explosions: The ejection velocity of pyroclasts. Geophysical Research Letters 39(2): L02301.

Thompson JB 1928. Tongariro National Park, annual report of the board. Department of Lands and Survey. House of General Assembly, New Zealand. Session C13.

Thouret JC, Lavigne F, Kelfoun K, Bronto S 2000. Toward a revised hazard assessment at Merapi volcano, Central Java. Journal of Volcanology and Geothermal Research 100: 479-502.

Tilling RI 1989. Volcanic hazards and their mitigation: progress and problems. Reviews of Geophysics 27(2): 237-269.

Tilling RI 2008. The critical role of volcano monitoring in risk reduction. Advances in Geosciences 14: 3-11.

Topping WW 1974. Some aspects of Quaternary history of Tongariro Volcanic Centre. Unpublished PhD Thesis. Victoria University of Wellington, New Zealand.

Tsunematsu K, Chopard B, Falcone J, Bonadonna C 2013. A numerical model of ballistic transport with collisions in a volcanic setting. Computers & Geosciences 63: 62–69.

Vanderkluysen L, Harris AJL, Kelfoun K, Bonadonna C, Ripepe M 2012. Bombs behaving badly: unexpected trajectories and cooling of volcanic projectiles. Bulletin of Volcanology 74(8): 1849–1858.

Wallace LM, Beavan J, McCaffrey R, Darby D 2004. Subduction zone coupling and tectonic block rotations in the North Island, New Zealand. Journal of Volcanology and Geothermal Research 109, B12406.

Wardman J, Sword-Daniels V, Stewart C, Wilson T 2012. Impact assessment of the May 2010 eruption of Pacaya volcano, Guatemala. GNS Science Report 2012/09. 90 p.

Wilson L 1972. Explosive volcanic eruptions II. The atmospheric trajectories of pyroclasts. Geophysical Journal of the Royal Astronomical Society 30(4): 381 – 392.

Wilson CJN, Houghton BF, McWilliams MO, Lanphere MA, Weaver SD, Briggs RM 1995. Volcanic and structural evolution of Taupo Volcanic Zone, New Zealand: a review. Journal of Volcanology and Geothermal Research 68: 1–28.

Woods AW 1995. A model of vulcanian explosions. Nuclear Engineering and Design 155(1-2): 345–357.

Yamagishi H, Feebrey C 1994. Ballistic ejecta from the 1988–1989 andesitic Vulcanian eruptions of Tokachidake volcano, Japan: morphological features and genesis. Journal of Volcanology and Geothermal Research 59(4): 269–278.

Zobin VM, Luhr JF, Taran YA, Breton M, Corte A, De La Cruz-Reyna S, Dominguez T, Galindo I, Gavilanes JC, Muniz JJ, Navarro C, Ramirez JJ, Reyes GA, Ursua M, Velasco J, Alatorre E, Santiago H 2002. Overview of the 1997–2000 activity of Volcán de Colima, México. Journal of Volcanology and Geothermal Research 117: 1–19.

APPENDICIES

APPENDIX A: VOLCANIC HAZARD MAPS AS A MEDIUM FOR HAZARD ASSESSMENTS

Volcanic hazard maps have been used for many years to assess and present actual and potential hazards (Sparks et al. 2013). Maps may present a single hazard or an amalgamation of hazards, depending on the need and use of the map. The level of detail in hazard maps can vary, depending on location and accessibility, available data, the needs of the audience and time (whether it is a crisis or non-crisis situation). For example in a crisis situation where ongoing eruptions are likely, the need for in depth hazard analysis may be superseded by the need for a rapidly produced, easy to understand multi-hazard map suitable for the general public. Whereas, a hazard map produced with greater time in a non-crisis event, designed to be read by scientists, will be more in-depth including modelled scenarios, probabilistic assessments and may be specific to a particular hazard.

Volcanic hazard maps may be prepared using various components including: (1) field surveys, aerial photo and remote sensing analysis of the geology, topography and the nature and extent of hazards; (2) review of historical data including scientific reports and articles, books, site investigations, maps, photos and media reports for hazardous events and their frequency and magnitude; and (3) modelling of possible future hazards based on past behaviour. This may be deterministic with set scenarios, or probabilistic using random variables to account for uncertainty such as BET or Monte Carlo analyses (Marker 2013).

Maps generally use zonation as a means to distinguish decreasing areas of hazard (Sparks et al. 2013). They may show maximum distance (e.g. ballistics, pyroclastic flows, lahars) or thickness (e.g. ashfall) and probability of occurrence of one or multiple scenarios, or may show susceptibility (the tendency of an area to be impacted by certain hazards – not including the moment of occurrence or potential damage or losses; Dominguez-Cuesta 2013), exposure (elements that may be affected by a hazardous event, usually encompassing temporal and spatial aspects; (Birkmann 2013)), or vulnerability.

APPENDIX B: ELECTRONIC APPENDIX

- (a) Orthophoto mapped crater locations and diameters
- (b) Raw fieldwork data
- (c) Modelled 200m-s no flow velocity data
- (d) Modelled 400m-s no flow velocity data
- (e) Modelled best fit (to the 6 August eruption) data
- (f) Modelled smaller eruption scenario data
- (g) Modelled magnitude larger eruption scenario data